Title

Convergent hydraulics at horseshoe steps in bedrock rivers

Journal

Geomorphology, 82(1-2)

ISSN

0169-555X

Authors

Pasternack, Gregory B
Ellis, Christopher R
Leier, Kyle A
et al.

Publication Date

2006-12-01

DOI

10.1016/j.geomorph.2005.08.022

Peer reviewed

Convergent hydraulics at horseshoe steps in bedrock rivers

Gregory B. Pasternack[a,*], Christopher R. Ellis[b], Kyle A. Leier[b], Brett L. Vallé[a], Jeffrey D. Marr[b]

[a]*Department of Land, Air, and Water Resources, University of California, One Shields Avenue, Davis, Ca 95616-8626, USA*

[b]*National Center for Earth-surface Dynamics, St. Anthony Falls Laboratory, University of Minnesota, 3rd Ave SE, Minneapolis, MN 55414*

*Correspondence to: Gregory B. Pasternack, 211 Veihmeyer Hall, Dept. of Land, Air, and Water Resources, One Shields Ave., University of California, Davis, Davis, CA, 95616 USA. E-mail: gpast@ucdavis.edu. Phone: 530-754-9243. Fax: 530-752-5262.

Abstract

Horseshoe waterfalls are a common feature of steep bedrock rivers. As a first step toward understanding their geomorphology, a detailed study of the fluid mechanics at a 0.91-m vertical-drop, horseshoe waterfall was performed in a 2.75-m wide flume. Five non-dimensional upstream energy levels, each with 3-5 non-dimensional downstream tailwater depths (21 runs total), were assessed for water surface topography via digital elevation modeling, flow dynamics via digital videography, and overall energy dissipation via an energy and momentum conservation model. Regardless of tail depth, the horseshoe waterfall was found to have three distinct zones beyond the step brink- 1) a nappe whose degree of convergence depends on upstream energy and brink configuration, 2) a convergence zone whose features vary strongly with upstream energy, brink configuration, and tail depth, and 3) a downstream tailwater region whose dynamics primarily depend on tail depth. The centerline nappe profile and brink velocity were reasonably predicted using Rouse's jet trajectory equations when (H+P)/H>2. Peripheral profiles were not predictable using existing equations. For any arbitrary broad-crested step brink configuration, maximum energy dissipation was found to occur when no jump was present and downstream tail depth was exactly critical. Rather than providing maximal energy dissipation, hydraulic jumps below steps provide efficient conversion of kinetic energy to potential energy.

Keywords: hydraulic jumps, waterfalls, mountain rivers, bedrock rivers, fluvial geomorphology

1. Introduction

A bedrock step in a mountain river is a nearly vertical drop in channel bed elevation, and depending on the geomorphic context may be termed a kickpoint, headcut, waterfall, bed sill, or downstep. High velocity and depth, cold water, unstable footing, and poor subsurface visibility hinder wading near bedrock steps at all but the lowest flows. Thus, step processes have been studied in flumes and scale models with 2-D geometries. However, natural steps have complex 3-D features that possess key mechanistic differences. A case in point is the horseshoe falls. In this study, aspects of the 3-D fluid mechanics of horseshoe falls at prototype scale are reported.

1.1 Previous Research

Before addressing horseshoe falls, bedrock step processes learned from prior field, flume, and dam studies are reviewed. First, due to the difficulties with making process measurements on steps, field studies have been limited to characterizing bedrock resistance (Moore, 1997; Sklar and Dietrich, 2001; Simon and Thomas, 2002) and channel morphology (Alexandrowicz, 1994; Wohl and Grodek, 1994) as well as estimating recession rates (Derricourt, 1976; Tinkler et al., 1994; Hayakawa and Matsukura, 2003) and scour hole sizes (Comiti et al., 2002; Lenzi and Comiti, 2003; Lenzi et al., 2003a). With regard to scour-hole morphology, Lenzi et al. (2003a) used field measurements to develop an empirical equation that predicts maximum clear-water, long-term scour depth and length for 2-D steps. Despite the challenges, steps are foci for intense erosion and likely play a key role in geomorphology, necessitating further field-based research.

Second, several studies have assessed cohesive-bed, 2-D headcut growth and migration by clear water for individual steps in 0.1-2.4 m wide flumes (Stein and Julien, 1993; Stein et al., 1993, Robinson and Hanson, 1996; Hanson et al., 1997; Bennett, 1999; Bennett et al., 2000;

Bennett and Casili, 2001; Alonso and Bennett, 2002; Stein and LaTray, 2002). Bed-material strength and channel hydraulics control headcut migration rate. Froude number and the aspect ratio of drop height to normal flow depth determine self-degrading versus self-propagating modes of headcut migration over a homogeneous cohesive-bed. Although useful for agricultural furrows and hillslope gullies, these results may not be extrapolated to bedrock rivers, because the experiments 1) used a significantly lower ratio of bed resistance to hydraulic forcing, 2) lacked comparable aeration and associated processes, and 3) lacked a bedload-dominated sediment transport regime. Flume studies have also been performed on the origin and evolution of cyclic 2-D steps (e.g. Parker and Izumi, 2000; Lenzi et al., 2002; Lenzi et al., 2003b).

Third, dam hydraulics research providing design guidance also offers insights into bedrock step mechanics. Key flow features that have been studied include aeration, internal flow structure and kinematics, energy dissipation, and scour dynamics. Hydraulic structures with well known fluid mechanics include sharp-crested/ogee-crested weirs (e.g. USBR 1948; Elevatorski, 1959; Leutheusser and Birk, 1991;Vischer and Hager, 1998), broad-crested weirs/abrupt drops (e.g. Rand, 1955; Robinson, 1992; Chanson and Toombes, 1998; Robinson et al., 2001; Mossa et al., 2003), and cascading steps (e.g. Chanson, 1995; Chanson, 2002). An important conclusion is that jet shear stress and dynamic pressure fluctuations are the primary erosional mechanisms for 2-D bedrock steps (Coleman et al., 2003). Bollaert and Schleiss (2003a) offered an excellent review of jet scour. Research quantifying pressure fluctuation processes include Fiorotto and Rinaldo (1992), Robinson et al. (2001), and Bollaert and Schleiss (2003b).

1.2 Horseshoe Falls Conditions

Significant differences between idealized 2-D and natural 3-D steps constrain direct use of existing theory to real rivers (Valle and Pasternack, 2001). In a river, bed slope and channel sidewalls may differ upstream, at, and downstream of a step. Steps are often irregularly shaped and may have a fractured, disjointed surface creating multiple scales of roughness and flow complexity. A step may be oblique to banks or oncoming flow. Its slope may deviate from vertical along the brink. Downstream of the step the bed may be incised into bedrock, strewn with boulders, or mantled with sediment. Finally, river steps contain varying amounts of suspended- and bed-load sediment particles that catalyze bed erosion (Sklar and Dietrich, 2001). For these reasons, accurate hydrodynamic and landscape evolution models that predict sediment transport and basin evolution require systematic studies of bedrock steps.

Despite the diverse complexity of bedrock steps, one morphology is widespread, highly significant for channel evolution, and tractable in a laboratory flume- the "horseshoe falls" (aka "U-shaped step" or "duckbill weir"). Niagara Falls in Canada is a well-known example (Tinkler et al., 1994). Shanghai Falls on the Feather River, CA (Fig. 1) is notable for its weakly cohesive bed, recession rate of ~5 m yr^{-1}, internal competition among multiple ∪'s, and influence of a meander bend on lateral morphology, with an abrupt step at the outer bend and a slide at the inner bend. One ∪ has captured the majority of flow and migrated farthest. Among hydraulic structures, curved ogee-crested dams, labyrinth weirs, and horseshoe weirs possess similarities useful for understanding natural horseshoe steps (Falvey, 2003).

The overall goal of this research was to investigate the Eulerian fluid mechanics and aspects of the Lagrangian flow kinematics of a broad-crested, 3-D horseshoe step in a rectangular channel. Objectives included (i) computation of overall energy dissipation provided by a broad-crested step with arbitrary crest planform as a non-dimensionalized function of

upstream energy and downstream submergence, (ii) generation and analysis of 3-D digital elevation models (DEMs) spanning the step unit (i.e. step top, step, and tail pool) for a variety of flow regimes, (iii) quantification of nappe profiles and ballistic kinematics for the free-falling, convergent jet along streamtubes, and (iv) description of 3-D flow dynamics downstream of a horseshoe step. Experiments were carried out at near-prototype scale with discharges up to 3.47 $m^3 s^{-1}$. Ultimately, this research addresses the problem of landscape evolution because it provides insight into constitutive hydraulics responsible for bedrock incision.

2. Step Systematics

2.1 Eulerian Governing Equations

Consider steady energy and momentum conservation for a control volume in a level rectangular channel with clear water including a broad-crested bed step of arbitrary brink configuration and the region downstream of the step (Fig. 2). Further, assume that the upstream total energy and the downstream tailwater depth are independently controllable. Then there hold for average conditions the overall energy conservation equation:

$$E_{up} = (H + P) = (h_d + h_{tail}) = E_{tail} + h_L \quad (1)$$

the definition of the submergence variable, h_d:

$$h_d = h_L + h_{v\_tail} = h_L + \frac{q^2}{2gh_{tail}^2} \quad (2)$$

the mass conservation equation:

$$q = v_i h_i \quad (3)$$

the critical flow condition:

$$h_c = \left(\frac{q^2}{g}\right)^{1/3} \quad (4)$$

the broad-crested weir equation:

$$q = (2/3)^{3/2} C_b \sqrt{g} H^{3/2} \quad (5)$$

the definition of Froude Number at location *i*:

$$Fr_i = \sqrt{\frac{q^2}{g h_i^3}} \quad (6)$$

the momentum equation applied between the upstream and nappe toe points for an unsubmerged jump condition (Henderson, 1966):

$$\frac{h_{toe}}{h_c} = \frac{\sqrt{2}}{1.06 + \sqrt{\frac{P}{h_c} + \frac{3}{2}}} \quad (7)$$

energy conservation equation at the nappe toe for an unsubmerged jump (Henderson, 1966):

$$\frac{E_{toe}}{h_c} = \frac{h_{toe}}{h_c} + \frac{h_c^2}{2h_{toe}^2} \quad (8)$$

the momentum equation applied between the nappe toe and the downstream tail point for an unsubmerged jump (Henderson, 1966):

$$r = \frac{h_{tail}}{h_{toe}} = 0.5\left(-1 + \sqrt{1 + 8Fr_{toe}^2}\right) \quad (9)$$

and energy dissipation through an unsubmerged jump (Henderson, 1966):

$$E_{tail} = E_{toe} - h_{toe}\left[\frac{(r-1)^3}{4r}\right] \quad (10)$$

where E_i and h_i are total energy and water depth at any location *i* as defined in Figure 2; H is the specific energy at the upstream location (weir crest as datum), P is broad-crested step height, q is specific discharge, h_L is total energy loss in the control volume, g is the gravitational constant, v_i is velocity at location *i*, and $C_b = 0.848$ is the broad-crested weir discharge coefficient (Ackers et al., 1978; Leutheusser and Birk, 1991; Chanson, 1999). In addition, the variable (H+P)/H is the

non-dimensional energy variable accounting for both discharge and step height (USBR, 1948). It shows that geometric scaling to yield any energy condition is achievable by holding either step height or flow constant. Higher (H+P)/H corresponds with taller steps with relatively less flow over them. In the lower limit of no step, the variable approaches unity.

2.2 Eulerian Energy Dissipation Regimes

The above equations have been solved for total energy and flow kinematics at the upstream, nappe toe, and tail locations associated with tailwater depth set to place the leading edge of the hydraulic jump exactly at the nappe toe, which was defined as "optimal" (Henderson, 1966). Critical depth non-dimensionalizes variables; however, locating the critical point introduces error (Ackers et al., 1978), whereas defining upstream specific and total energy is more practical and certain. Energy loss increases as a function of step height relative to specific energy (Fig. 3). The majority of energy loss occurs at or before the nappe toe (Fig 3). As E_{up} and h_L increase, the fraction of E_{up} dissipated by the hydraulic jump approaches a limit of ~0.26, while that upstream of the jump approaches ~0.62, leaving $E_{tail} \approx 0.12\ E_{up}$. The primary mechanisms for this non-jump energy dissipation are fluid momentum transfer under the nappe (White, 1943) and transfer of energy into the bed. Bed scour, water-air momentum transfer, and heat and sound generation are secondary h_L mechanisms. Transmission of energy into the bed occurs as seismic waves that propagate through the ground and eventually dissipate.

The solution for flow kinematics and energy loss for an optimal jump illustrates the relative role of a hydraulic jump in energy dissipation at river steps, but fails to consider the controlling role of h_{tail}. For a dam spillway, jump location and h_{tail} are often controlled by energy dissipators (Chanson, 1999), so the general solution for any arbitrary h_{tail} was not needed. For a

bedrock river h_{tail} is rarely optimal and varies as a function of longitudinal channel profile, discharge, and geology. In this study, "submergence" is defined as the condition when h_{tail} is deep enough to place the leading edge of the jump upstream of the location of the free-falling nappe toe. Equations 7-10 do not apply to a submerged hydraulic jump.

Mathematica 4.1 was used to solve equations 1-6 for fractional energy dissipation $h_L/(H+P)$ for a range of submergence h_d/H and energy $(H+P)/H$. Upstream Fr is not independent in a river, but may be controlled in a flume using a sluice gate. The resulting contour plot of $h_L/(H+P)$ as a function of h_d/H and $(H+P)/H$ shows that the optimal-jump solution (Fig. 4, line B) is a subset of the general solution. Maximum $h_L/(H+P)$ for any $(H+P)/H$ occurs when h_{tail} is exactly critical with no hydraulic jump present (Fig. 4, line A). This maximum involves a transition from supercritical to critical flow and $h_{toe}<h_{tail}$. Also, as h_{tail} is decreased to less than critical depth, $h_L/(H+P)$ decreases and the flow increases its efficiency until $h_{toe}=h_{tail}$. The primary conclusion from this analysis is that h_{tail} is an essential element of flow kinematics and energy dissipation at river steps, and this was key to the study's experimental design.

Consider whether the planview shape of the step brink affects h_L and flow kinematics at upstream and tail cross-sections. According to equations 1-6, when $(H+P)/H$ and h_d/H are specified, the resulting $h_L/(H+P)$ and flow kinematics at upstream and tail cross-sections are independent of step brink geometry. Thus, this study addresses the role of step brink geometry in controlling internal fluid mechanics relevant to bed scour, water quality, and aquatic habitat.

2.3 Nappe Profile Equations

Flow kinematics for the nappe derive from semi-empirical nappe profile and ballistic equations for each step geometry. No equations exist for a horseshoe weir. Radial flow toward a

radial "Morning Glory" intake yields upper and lower nappe profiles mimicked by the equations of Vischer and Hager (1998). These equations scale H to intake radius, which may be important for horseshoe steps of varying eccentricity. Analysis of the horseshoe step is complicated due to the momentum of linear flow in a rectangular channel with a radial bed step. At the channel centerline, one expects little deviation in nappe profile relative to a 2-D rectangular step. For this profile, Rouse's (1957) equation given as

$$z = -\frac{g}{2V_b^2}x^2 + c_1 \quad (11)$$

where x and z are coordinates relative to the brink location, V_b is the velocity at the brink, and c_1 is an integration constant equal to the water surface elevation at the brink(z_b) was tested.

3. Experimental Setup and Methods

3.1 Experimental Design

The goal was to characterize the convergent hydraulics of a broad-crested horseshoe step with a plunging nappe. The independent variables were non-dimensional energy (H+P)/H and non-dimensional submergence h_d/H. For a broad-crested step, supercritical brink Fr is constant for all (H+P)/H, so both geometric and Froude scaling was achieved. Flume dimensions and step height were prototype scale for creeks. Aeration was present in all runs.

One consequence of a horseshoe brink is that the previous definition of submergence is not valid. Starting with h_{toe}=h_{tail} and holding E_{up} constant, as h_{tail} is increased, an undular jump forms and propagates upstream to the step. When the leading edge of the jump passes the nappe toe at the downstream periphery, submergence is initiated and the undular jump becomes a hydraulic jump. More nappe toe is submerged with increasing h_{tail} until a threshold h_{tail} is

reached that submerges the centerline toe. In this study only conditions with either completely unsubmerged or submerged nappe toes were evaluated.

Twenty-one combinations of the two controlling variables were investigated (Table 1). For each (H+P)/H there was one supercritical h_d/H run, one highly submerged h_d/H run, and 1-3 runs with intermediate h_d/H (Fig. 4, points). Cross-sectionally averaged kinematics for these runs were predicted with equations 1-6 (Table 1). All runs involved a nappe whose toe was at a lower elevation than the step crest elevation. Undular and sloping jump conditions present at very low values of h_d/H were not investigated.

3.2 Flume Facility

All tests were done in a non-recirculating, non-tilting, concrete and steel flume 84-m long x 2.75-m wide x 1.8 m deep at University of Minnesota's St. Anthony Falls Laboratory (Minneapolis, MN, USA), (Fig. 5a). This facility supplies Mississippi River water over an adjustable range of 0-8.5 $m^3 s^{-1}$. A hollow-wood broad-crested step 4.28-m long x 2.75-m wide x 0.91-m high was bolted ~60 m downstream of the flume's inlet and coated with smooth paint. It was situated partly over a steel-plated, false-floor section with a glass sidewall. At the downstream end of the step, an additional 1.37-m section of joist-supported, 2-cm thick painted plywood was cantilevered out with a semi-circular area cut out yielding a ∪-shape (1.37 m radius = channel half-width). The ratio of brink length to channel width for this configuration was π/2. The horseshoe was also supported by a 10 cm x10 cm wood pier at each downstream peripheral tip. Under the horseshoe, ventilation was provided to minimize nappe oscillations using a 2.54-cm dia. aluminum pipe through the floor. In nature, the multi-scalar roughness on a

step locally disturbs the nappe or nappe-bank boundary providing ventilation. An adjustable sharp-crested weir at the downstream end of the flume was used to control h_{tail}.

3.3 Data Acquisition

The needed data were discharge (Q), bed coordinates, and water surface coordinates. To measure and set Q for each run, the broad-crested step method was used (Ackers et al., 1978). H, h_{up}, and Q measurements upstream of the step were unaffected by the horseshoe downstream of the critical point. The discharge constant was 0.848 (British Standard). P, step length L, and h_{tail} were within the range of a constant discharge coefficient. Once the H- h_{up}-Q relation was known, Q was set for each run using the inlet gate to provide the necessary upstream stage, which was monitored with a staff gage and converted to H. Q was nearly steady during each run.

A triangular truss was fixed level on a rolling carriage over the flume (Fig. 5b). A small "rover" carriage set on the truss could be positioned along it and locked down. A 2.565 m long x 2.54 cm diameter aluminum pole with a fine tip at the bottom and a surveying prism (1" accuracy glass) mounted on top was placed into a leveled bushing unit on the rover. The pole was raised and lowered with a winch. In addition to the winch, a spring-loaded brake prevented the pole from moving due to violent bursts of flow. This system accurately located the 3-D coordinate of any chosen point.

A Topcon GTS-603 total station was used to measure bed and water surface topography. This unit had a 3-sec resolution with a distance (D) accuracy of ±(2 mm+2ppmxD) mean square error. It was located at a single point within 15 m of the step to minimize error. A TDS Data Collector was used to collect and edit survey data and descriptions. A local coordinate system

was established along the flume with a {304.8 m, 304.8 m, 30.48 m} X,Y,Z datum set near the tail weir and used as the backsight. Control points were used to test accuracy and precision.

A consistent method was used for all runs. The flume carriage was positioned at one end of the reach with the rover along one wall. Longitudinal water surface profiles spaced 0.3-m apart were surveyed using a feature-based approach (e.g. Lane et al., 1994; Brasington et al., 2000). A grid was used where no features were visible. For the steep nappe, a point was taken for ~8 cm of vertical change in water surface position. Grade breaks were surveyed at the step rim, nappe toe, and around shockwave "rooster tails". Supplemental feature-based surveying provided higher density point sampling to resolve "rooster tails" and "boils". For each discharge, the step top and upper nappe were only surveyed at lowest h_{tail}. The lower nappe, flow convergence zone, and downstream tail water zone were surveyed for all runs. Accuracy checks were performed ~5-10 times during the ~3-4 hour period of a run. Mean accuracy was 7.15 mm (± 3 mm SD) horizontal and 1.95 mm (±1 mm SD) vertical.

Determination of the water surface elevation with a point gage in extremely turbulent, bubbly, even spraying flow conditions was nontrivial. For step top, nappe, and tail-region points the water surface was easily located within 1-3 mm. In the jump region, the water surface elevation at a point could vary by as much as ~0.50 m over a few minutes at the lowest (H+P)/H. Long-duration monitoring of each point with a water-contact sensor was not practical. Instead, a key indicator of the mean water surface elevation was the duration between drips of water off the point-gage tip. Lack of drips indicated excessive or deficient submergence. Equal durations of submergence and straight-down dripping were used as an objective and consistent measure of time-averaged water surface elevation. For supercritical spray-jets, the method was to begin

fully submerged and raise the tip until drips began to fall straight down. Thus, the primary uncertainty in the data stems from the time variation of violent, bubbly flow.

To characterize flow pattern, visual observation, digital photography, digital videography, and cross-sectionally averaged velocities were used. Given the short duration of access to the flume, detailed mapping of point velocities and other flow variables was not possible. The obtained observations provided qualitative flow information that was helpful in understanding flow mechanics, but further process studies are warranted.

3.4 Data Analysis

AutoCAD 2002 Land Desktop was used to create scaled water surface DEMs. The elevation of the lowest bed point was subtracted from each point *i* to obtain Z_i, the water surface above datum. Then Z_i/H was calculated for comparisons across runs. The {X, Y, Z_i/H} datasets were imported into AutoCAD to make DEMs using a triangular irregular network algorithm. DEMs were built with the aid of step-rim, nappe-toe, "rooster tail", and "boil" breaklines. A Z/H contour interval of 0.15 was used as a compromise between resolving hydraulic jump water surface topography and oversaturation with nappe contours. Significant features at the sub-0.15 Z/H level are only described in the text and shown in centerline profiles. Individual planform and 3-D metrics were obtained using AutoCAD's analysis tools. AutoCAD's Civil Add-on was used to obtain non-dimensional X/H versus Z_i/H centerline profiles.

4. Results

DEMs and videos captured the 3-D spatial flow structure over the horseshoe step of varying (H+P)/H and how flow features changed with h_d/H. The 3-D flow structure was found to

be composed of 3 distinct regions- the nappe, the flow convergence zone, and the downstream tailwater zone. Details are only provided for the first set of runs with (H+P)/H=5.55. After that, the focus is on unique aspects of each (H+P)/H, with Table 2 and DEMs summarizing results. Care was used when cross-comparing DEMs (dimensional X and Y) and centerline profiles (non-dimensional X/H). All analyses used non-dimensional Z/H.

4.1 (H+P)/H=5.55 runs

Photos, videos, and DEMs for the tallest step show a wide range of 3-D flow features, including horseshoe nappes, spray jet domes, shockwaves, boils, and hydraulic jumps (Fig. 6). The cross-sectionally averaged Fr measured at the brink apex was 1.67. Thus, nappe mechanics were controlled by E_{up} and brink geometry. For increasing h_{tail}, the nappe toe showed a lateral and vertical progression toward the brink (Table 2). Except when h_{tail} was supercritical, $h_{toe}<h_{tail}$. Supercritical shockwaves yielded $h_{toe}>h_{tail}$.

Planform analysis of the nappe showed the effect of step-brink geometry and h_{tail} on nappe profile and initial flow convergence. The ratios of mean nappe contour length to channel width and mean nappe contour length to step brink length for the fully exposed nappe at the lowest tail depth were 1.274 and 0.811, respectively. 2-D rectangular flow would have both ratios equal to 1. 3-D radial flow would have them equal to $\pi/2$ and 1, respectively. These values correspond with higher 3-D brink discharge than cross-sectional Q. Also, they show that streamtubes through the nappe did not converge to be perpendicular to the brink as would be expected for potential flow, due to the longitudinal momentum of the approach flow. Both ratios were lowest at the brink, increased 12.4% down the nappe to a location 0.241H from the brink position, and then decreased 5.6% down to the nappe toe. When tailwater fully submerged the

nappe toe, water pushed against the nappe, but nappe curvature did not change near the nappe toe centerline. It did increase along the wall where nappe velocity was low and h_{tail} was higher.

The most significant effects of horseshoe geometry and tail depth were observed in the flow convergence zone downstream of the nappe toe. When h_{tail} was supercritical, this zone showed two structured subregions- a spray jet dome and a "rooster tail" (Fig. 6a,c). Upon striking the bed, some flow was forced under the nappe, but most rebounded into a converging, domal spray jet (Fig. 6c). Supercritical skimming flow occurred under the spray jet. The peak of the jet occurred 2.694H downstream of the nappe toe along the centerline and had a Z/H=1.370. Flow converging onto this apex included 42% of the total flow. Most of the remaining jet subsequently converged at a point 9.40H downstream of the nappe toe yielding a superposed shockwave "rooster tail" with an apex Z/H of 1.695. The remaining peripheral jet impacted the side of the rooster tail forming a localized 3-D hydraulic jump on each side. Jump strength decreased toward the wall, where flow came from the pool under the nappe, escaping where the nappe detached from the wall. Escaping flow diverged and accelerated as it moved downstream to fill the void caused by the converging nappe flow. The supercritical depth for each peripheral jump was 0.30H, which was significantly less than h_{toe}, presumably due to the lateral flux to the domal spray jet. As flow through the rooster tail diverged downstream, some of it impacted the wall and was deflected back upstream along the wall forming a peripheral eddy (Fig. 6a) that set h_{tail} (Z/H=0.45-0.6) for the localized jumps along the rooster tail.

Downstream of the rooster tail, flow diverged strongly, depth decreased, and a repeating sequence of diverging and converging shockwaves was evident (Fig. 6a). The sharp water-surface topographic transitions of these waves were not surveyed in detail, but peripheral peaks and a central trough occur in the DEM where $Z/H \geq 0.60$ and $Z/H \leq 0.30$, respectively (Fig. 6c).

The peripheral peaks were in line with nappe streamtubes, but did not result from flow crisscrossing. They stem from divergence of the flow leaving the rooster tail. Shock waves were present downstream to the end of the flume.

Starting with a supercritical h_{tail}, increasing h_{tail} yielded dramatic changes to flow features. Initially, peripheral jumps adjacent to the rooster tail became stronger and moved upstream. When they intersected the nappe along the periphery, they merged into a single continuous jump across the spray jet subregion upstream of the rooster tail. Increasing h_{tail} led to an increasing length of peripheral submergence of the nappe toe. The h_{tail} threshold for full submergence of the nappe toe was measured to be $h_{tail}/H=1.60$ ($h_d/H=3.95$), whereas that for a 2-D rectangular step was calculated to be 1.335 ($h_d/H=4.215$; Fig. 4). Under this condition, the domal spray jet subregion was transformed into the upstream-facing slope of a channel-wide hydraulic jump.

Along with photos and DEMs, centerline profiles illustrate changes in water surface topography with h_{tail} (Fig. 7a). At $h_{tail}/H=0.32$ ($h_d/H=5.23$), spray jet and rooster tail subregions were highly differentiated and $h_{tail}<h_{toe}$. With increasing h_{tail}, profile changes included shifting of the nappe toe upstream, merging of the spray jet and rooster tail into a single hydraulic jump region with a hydraulic "boil", and changing in the sign of the water surface slope in the downstream tailwater zone. The change from a rooster tail to a boil was a result of a partial drowning and reduction in flow momentum in the convergence zone. Whereas the rooster tail had unidirectional downstream flow along the centerline of the X-axis, boils had bidirectional flow, with a downstream current underlying a surficial upstream current. The boil's topographic relief was highest for the least submerged run and decreased with increasing h_{tail} relative to the tail and nappe-toe water surface basal elevations. Even though this relief might suggest that the surficial reverse flow would be strongest for the lowest submergence run due to the

potentiometric gradient, the opposite was observed in videos, because the lowest submergence run provided the least reduction in depth-averaged (net-downstream) velocity. Thus, the strength and length of bidirectional flow increased with increasing h_{tail}. The location of the boil apex shifted upstream and up with h_{tail} (Table 2). Boil apex $Z/H > h_{tail}/H$ always (Fig. 7a).

More 3-D boil features were observed in DEMs, photos, and videos in the hydraulic jump region. Surficial reverse flow down the upstream face of the boil impacted the converging submerged jet coming off the nappe (Fig. 6b). This resulted in a ∪-shaped frontal depression at the fluctuating interface between the two. For $h_{tail}/H=2.50$, imagery show a peripheral plateau between the nappe toe and the boil apex where the downstream-directed flow was bunched up by the reverse flow and a surficial foam layer was present. This plateau was followed by a depression at the interface itself, which also had a line of bubbles along it (Fig. 6b). The topography of the undulating depression was partially captured in the DEM as two circular depressions between the peripheral plateaus (Fig. 6e). For the highest h_{tail}, the plateau was fully connected around the ∪-shape due to the decreased depth-averaged velocity of flow along the centerline at this higher h_{tail}. The plateau and downstream depression were fully captured in both the DEM (Fig. 6f) and in the centerline profile (Fig. 7a). The depression extends downstream of the step because there is a flow interface there as well, though of different cause. In this area, h_{tail} was high enough to quench the surficial downstream velocity of the flow along the wall coming from the pool under the nappe. As a result, the primary flow direction in this area was transverse to the channel along the potentiometric gradient of the boil. The transverse flow and resulting piling up of water at the wall were evident in the video.

With supercritical h_{tail}, the downstream tailwater zone had a negative water surface slope, whereas with a subcritical h_{tail} it had a positive slope (Fig. 7). The length and height of the rise

decreased with increasing h_{tail}. No significant lateral variation in Z/H was observed in the subcritical downstream tailwater zone despite sufficiently dense sampling (Fig. 6d,e,f).

4.2 (H+P)/H=4.75 runs

Photos and DEMs for the second-to-highest (H+P)/H show many similar features to those present for the highest (H+P)/H set and some differences in details (Table 2, Figs. 7-8). Unique aspects of the nappe included a flattening of the dimensional nappe profile and decreases in the ratios of mean contour length to channel width (1.262) and mean contour length to step brink length (0.803). Non-dimensional centerline coordinates of the nappe toe shifted upstream and up, but showed the same trend with increasing h_{tail} (Table 2). For supercritical h_{tail}, the flattening of the nappe planform curvature resulted in a wider and non-dimensionally shorter spray jet dome in the convergence zone (Fig. 8b,c). The distance from the nappe toe to the jet's apex was 3.49H and the jet's apex had a Z/H=1.297 (Fig. 7b). The rooster tail was dimensionally wider and longer (Fig. 8b,c) but non-dimensionally further upstream, with its apex 7.62H downstream from the nappe toe and its Z/H=1.554 (Fig. 7b). Peripheral hydraulic jumps were stronger and spanned from the channel wall to the side of the rooster tail. More supercritical outflow diverging from the under-nappe pool along the walls yielded a sharper jump transition to the pool caused by rooster tail backflow (Fig. 8b,c). Shockwaves were present down the flume, with peripheral highs pushed further downstream.

As h_{tail} was increased, a similar response of boil development and migration was observed as for the highest (H+P)/H runs (Figs. 7, 8). Submergence of the center of the nappe toe occurred at h_{tail}/H= 1.515 (h_d/H=3.235), whereas that for an optimal 2-D jump was calculated to be h_{tail}/H= 1.288 (h_d/H=3.462). Relative to the lowest-energy runs, the front between

downstream jet flow and upstream boil flow for these runs was non-dimensionally longer with a longer foam layer (Fig. 8a). Also, the relief between boil apex Z/H and h_t/H was reduced and the velocity of surficial reverse flow was higher.

The onset of the peripheral plateau in the hydraulic jump region was not captured in this set of runs, but other interesting effects were recorded. No such plateau was observed for h_{tail}/H=1.74 (Fig. 8d), because the downstream velocity was high enough to limit surficial flow reversal. By h_{tail}/H=2.35 the plateau was present along the full nappe toe (Fig. 7b, 8e) and strong flow reversal was visible. In the (H+P)/H=5.55 runs, the plateau had not reached the centerline by even h_{tail}/H=2.50 at which point the downstream cross-sectionally averaged velocity was significantly lower than for this case with h_{tail} /H=2.35. The discrepancy may be explained by the reduced convergence of flow and resulting reduced centerline velocity for the lower (H+P)/H run as indicated by the significant difference in boil relief (ΔZ/ΔH) relative to the nappe toe between the higher and lower (H+P)/H runs, with the relief being 0.537 and 0.392, respectively (Figs. 6e, 8e). No downstream extension of the frontal low was evident in this run as had been observed for (H+P)/H=5.55 with h_{tail}/H=3.67, because the decreased convergence and higher energy yielded a much higher velocity for outflow diverging from the pool under the nappe. It also yielded higher velocity for peripheral nappe flow. These velocities were high enough to prevent the boil's transverse flow from having an effect until further downstream, where water piling up against the wall was recorded in the pattern of the 2.25 Z/H contour line in Figure 8e. For h_{tail}/H=3.30, no downstream frontal low was observed for the same reason (Fig. 8f). However, this run showed a wide central plateau with narrow peripheral plateaus and large depressions between them (Fig. 8f). In this case, the velocity of the surficial reverse flow was higher and accelerating toward the nappe toe yielding a decreased depth between the boil and

plateau. At the same time the greater flow along the channel periphery due to the higher upstream energy produced strong submerged jets directed toward the channel center. These accelerated and decreased in depth toward the channel center forming the depressions. These peripheral jets had the same strength at all h_{tail}, but at a low h_{tail} their strength relative to that of the main downstream flow was small. Consequently, at low h_{tail} the peripheral jets were swept downstream by the main flow, while at high h_{tail} the main flow in the convergence zone had significantly decreased net-downstream flow and the submerged jets have a much greater impact.

4.3 (H+P)/H=4.0 runs

Hydraulics for (H+P)/H=4.0 showed more incremental changes in all step regions. In the nappe region of the supercritical h_{tail} run, the profile flattened more and the nappe planform had less curvature, with a mean nappe contour length to channel width ratio of 1.22 and a mean nappe contour length to step brink length ratio of 0.776. In the convergence region, a spray jet sub-region was still present, but the spray arced at a much lower angle with much less converging on a dome-shaped center (Fig. 9a). The apex of the spray jet was only Z/H=1.0 due to the decreased convergence. The rooster tail was even longer and its peak was located further upstream (Table 2) to the point that the centerline spray jet tail was almost completely intercepted by the rooster tail (Fig. 7c). Water flowing out from the pool under the nappe accelerated to supercritical velocities and dropped to Z/H<0.3 more quickly yielding a larger area of skimming supercritical flow upstream of hydraulic jumps peripheral to the rooster tail (Fig. 9a). The tail region showed less accentuation in shock wave topography (Fig 9a).

More tail depths were assessed at this (H+P)/H to enable better cross-comparison, but overall, submergence yielded similar results to those already mentioned (Table 2; Fig 7c).

Whereas the least submerged subcritical h_{tail} for each of the higher (H+P)/H were fairly submerged, in this case h_{tail}/H for the equivalent run was 1.46 (h_d/H=2.54). This was close to the observed optimal position (h_{tail}/H= 1.453, h_d/H=2.547). For reference, the optimal 2-D jump in this case was calculated to be h_{tail}/H= 1.238 (h_d/H=2.762). At h_{tail}/H=1.46 the boil had sharp relief with little bidirectional flow. Peripheral submerged jets were swept downstream and played little role. At h_{tail}/H=1.99, an asymmetric peripheral plateau was observed with a small high area through the nappe center (Figs. 7c, 9c). Increasing h_{tail}/H to 2.62 yielded a migration of the plateau deeper into the jump region. For $2.62 \leq h_{tail}/H < 2.86$ the accelerating flow reversal and strengthening submerged peripheral jets pushed Z/H down along the periphery (Figs. 7c, 9d). For h_{tail}/H=2.86 the plateau was again localized in the channel center with a pattern very similar to that reported for (H+P)/H=4.75 with h_{tail}/H=3.33 (Figs. 7c, 8f). Peripheral submerged jets were very strong in this run. They delineated the capture zone of the submerged hydraulic jump.

4.4 (H+P)/H=3.0 runs

A hydraulic threshold affecting the spray jet subregion was crossed when E_{up} was further increased. Significant flattening of the nappe profile and planform was evident (Fig. 10a). The mean nappe contour length showed accelerated nonlinear decreases relative to channel width (1.19) and step brink length (0.76). At a supercritical h_{tail}, there was no spray jet or dome structure present along the central 70% of the nappe toe line (Fig. 10a). This subregion had non-aerated skimming flow with intermittent spraying. Spray jets were still present along the periphery where there was less flow than at the center. These jets impacted the side of the dimensionally wider and longer rooster tail. The apex of the rooster tail was non-dimensionally

further upstream with lower relief (Table 2; Fig. 7d). The pool under the nappe was deeper and its outflow accelerated along an elongated ramp into stronger peripheral jumps (Fig. 10a).

The effect of increasing h_{tail} on flow features at this (H+P)/H was similar to that seen for other (H+P)/H runs, but with further incremental changes. The boil's apex shifted even further upstream (Table 2), reverse flow increased even further in strength, and peripheral submerged jets had even higher velocity transverse to the channel. Submergence of the central nappe toe occurred at $h_{tail}/H=1.341$ ($h_d/H=1.659$), whereas the optimal 2-D jump would occur at $h_{tail}/H=1.16$ ($h_d/H=1.84$). All submerged runs had the same flow pattern consisting of a centralized plateau surrounded by lower regions where reverse flow accelerated toward the nappe toe (Figs. 7d, 10b-e). A h_{tail}/H of 1.58 had a plateau too (Fig. 7d), but it was not resolved in the DEM with Z/H contour intervals of 0.15. Peripheral submerged jets again played an increasing role in converging reverse flow upstream of the boil apex with increasing h_{tail}.

4.5 (H+P)/H=2.0 runs

At the lowest (H+P)/H several new features were observed. The nappe profile and planform were the most 2-D and the space under the nappe was fully submerged. The mean nappe contour length showed accelerated nonlinear decreases relative to channel width (1.10) and step brink length (0.7). At supercritical h_{tail} no spray jet occurred. Flow across the central 67% of the channel downstream of the step occurred as non-aerated supercritical flow. Flow along the wall stemming from under the nappe was deep (Fig. 11a,c), extended downstream almost adjacent to the rooster tail apex, and then accelerated to supercritical. The rooster tail had very low relief and flow diverging from it did so at a low angle. No upstream flow reversal was

observed along the walls (Fig. 11a,c), so no localized jumps were present adjacent to the rooster tail- the flow remained supercritical and directed downstream.

Two submerged h_{tail} were studied. The first was $h_{tail}/H=1.09$ (Fig. 11d), which was very close to the observed optimal h_{tail} ($h_{tail}/H= 1.084$, $h_d/H=0.916$). For reference, the optimal 2-D jump would occur at $h_{tail}/H= 1.053$ ($h_d/H=0.947$). For $h_{tail}/H=1.09$ there was no plateau or frontal depression in the jump region (Figs. 7e, 11d). The boil's apex was higher than the step brink (Table 2). At random intervals, depressions formed near the nappe toe and move downstream. The origin of such depressions were difficult to discern, but appeared to result from fluctuations in the air entrainment rate that yielded large air pockets in the flow. Higher velocity bursts followed the depressions, forming waves that rose and fell over the depressions in anywhere from 0.17-0.53 sec depending on wave size. At $h_{tail}/H=1.26$ no boil apex was observed (Fig. 11b) and none was evident in the DEM (Fig. 11e) or centerline profile (Fig. 7e). In this case, peripheral submerged jets dominated jump hydraulics and impacted each other in the channel center. The topography of the jump region was saddle-shaped, with lowest lows at accelerating peripheral jet areas, highest highs at the nappe toe and downstream tail areas, and a saddle center where the two peripheral jets impact at the channel centerline in the middle of the hydraulic jump region. At random intervals a large underwater air pocket was observed to originate near the nappe toe and burst through the converging transverse flow of the peripheral jets. Downstream of the step Z/H continuously increased with increasing X/H (Fig. 7e).

5. Cross-comparisons

The experimental design enabled cross-comparison of runs holding different variables constant. The results of holding upstream energy constant and varying h_{tail} were already

described. Comparisons were also done holding either h_d/H or h_{tail}/H constant. To help explain the differences observed in DEMs and videos, predictions of fractional energy dissipation $h_L/(H+P)$ and cross-sectionally averaged non-dimensional tailwater velocity head (h_{tail_vel}/H) were made using the model described in subsection 2.2 and illustrated in Figure 4.

5.1 Cross-comparison of runs with same h_d/H

The response of the horseshoe step to the effect of differing (H+P)/H and h_{tail}/H values for runs of the same h_d/H was observed for two different h_d/H values. In the first case $h_d/H \approx 3.03$ (Figs. 6e, 8d). The higher (H+P)/H run (Fig. 6e) had a much higher $h_{tail}/H=2.5$, so the amount of $h_L/(H+P)$ possible from the brink to the tail had to be much lower. For this run $h_L/(H+P)$ and h_{v_tail}/H were predicted to be 0.54 and 0.017, respectively. For the lower (H+P)/H run with a lower $h_t/H=1.74$, the predicted $h_L/(H+P)$ was 0.62 (Fig 4, {4.75, 3.05}). Despite having a greater fraction of energy dissipation, the lower (H+P)/H run had a higher h_{v_tail}/H of 0.035, because in the higher (H+P)/H case the preserved energy was in the form of depth, not velocity head. Because it had a lower velocity head, the higher (H+P)/H run was not able to push the tailwater back away from the nappe toe to the same degree, thereby resulting in the peripheral plateaus reported earlier (Fig. 6e). In contrast, the lower (H+P)/H run had a higher velocity head that was more capable of pushing off the tailwater to prevent the buildup of such a plateau (Fig. 8d).

In the second case of constant h_d/H, 3 runs were performed with $h_d/H \approx 1.42$ (Figs. 8f, 9d, 10c). As a function of decreasing (H+P)/H, these runs had decreasing h_{tail}/H and increasing $h_L/(H+P)$ and h_{v_tail}/H. The runs showed a progression of decreasing relative strength of their peripheral submerged jets resulting in a wider central plateau in the hydraulic jump region. One might expect that lower (H+P)/H with less convergent downstream flow should yield stronger

peripheral jets, but h_{tail} decreases significantly with the decreasing (H+P)/H, and this latter effect overwhelmed (H+P)/H and convergence effects. Thus, h_{tail} was found to be a significantly stronger control on jump hydraulics than (H+P)/H across this range. Again, higher fractional energy dissipation was associated with less submergence and higher tail velocities.

5.2 Cross-comparison of runs with same h_{tail}/H

The response of the horseshoe step to the effect of differing H and h_d/H values for runs of the same h_{tail}/H was observed for 3 different h_{tail}/H values- 0.33 (Figs. 6c, 8c, 9a, 10a, 11a), 1.44 (Fig. 9b, 10b) and1.74 (Figs. 8d, 10d). For both cases of $h_{tail}/H > 1.0$, the dynamics were similar, so the details are presented for $h_{tail}/H=1.74$. The higher (H+P)/H run (Fig. 8d) was used in an earlier cross-comparison ($h_d/H \approx 3.03$). For a constant h_{tail}/H, the higher (H+P)/H run had much higher $h_L/(H+P)$- 0.62 versus 0.41- and a slightly lower h_{v_tail}/H- 0.348 versus 0.353. Given that the two runs had the same h_{tail}/H and very similar h_{v_tail}/H, why did the higher (H+P)/H run with higher $h_L/(H+P)$ have more water surface relief and no plateau near the nappe toe? The answer is that the higher (H+P)/H run had much more flow convergence yielding much higher depth-averaged velocities in the jump region capable of inhibiting boil flow reversal. The lower (H+P)/H run had less flow convergence and a strong boil flow reversal. The high velocity core in the higher (H+P)/H case decelerated and thickened as it moved toward the tail, at which point the runs had very similar non-dimensional conditions, though this transition could not be calculated. Thus, for a given h_{tail}, a more submerged jump is a poorer energy dissipater, but a more efficient converter of kinetic energy to potential energy.

For the supercritical runs, all (H+P)/H yielded an $h_{tail}/H \approx 0.33$ due to tail gate geometry. Many of the similarities and differences among these runs were already detailed. Figure 4 shows

that increasing (H+P)/H for a constant h_{tail}/H yields increased $h_L/(H+P)$. Although it is difficult to see in Figure 4, the rate of increase as a function of (H+P)/H for a constant h_{tail}/H is identical for supercritical and subcritical flow. Even though flow is supercritical, a similar effect was observed as for the subcritical runs in that higher $h_L/(H+P)$ for higher (H+P)/H runs yielded more water surface topographic relief due to an increased degree of flow convergence.

6. Centerline Nappe Profile Prediction

Non-dimensional centerline nappe profiles for all (H+P)/H values were compared against Eq. 11 to test whether horseshoe-step centerline profiles are 2-D (Fig. 12). All profiles showed the same shape, but the length of the profiles decreased with decreasing (H+P)/H. Eq. 11 was a good fit except for (H+P)/H=2, whose measured profile was much steeper than the other profiles for a similar range of X/H or predicted by Eq. 11 (Fig. 12). In this deepest case, surficial water going over the brink would behave as a free body, but a water parcel at the bottom of the thick flow would experience both its own weight and the pressure imposed from above. This would result in an added vertical (downward) force beyond the brink not accounted for in Eq. 11.

Centerline brink velocities calculated from Eq. 11 were compared against cross-sectionally averaged velocities for the same location calculated using Eq. 3. The (H+P)/H=4 profile matched Eq. 11 best, with the predicted velocity within 3% of that required by mass conservation. For (H+P)/H=4.75 and 3, Eq. 11 was within ~10 %. For (H+P)/H=5.55 the error was 29%. The worst error of 52%was for the worst matching profile of (H+P)/H=2.

When all data were collapsed to the same datum, a single fit of Eq. 11 provided a good match (Fig. 12b). The estimate of brink velocity for (H+P)/H=4 improved to within 0.5% using this equation. That for (H+P)/H=2 improved to within 43%, which was still poor.

7. Discussion

It is a common misconception about mountain rivers that increasing energy dissipation corresponds with decreasing velocity. This study demonstrates that most energy dissipation at steps stems from potential energy losses, not velocity head losses. A loss of H=1 m can be achieved by h_d>1 m or a corresponding but unlikely velocity decrease of >4.43 m s^{-1}. The maximum energy dissipation for a given step occurs when Fr_{tail}=1 and no hydraulic jump is present (Fig. 4). Hydraulic jumps below steps are thus not the primary means of energy dissipation, but are rather the mechanism for efficiently converting the high kinetic energy associated with steeply sloped channel units back to potential energy. The h_{tail} set by the geometry of the downstream channel unit controls the step's jump regime and thus how much of energy conversion takes place. For bedrock channels with little clear-water scour, energy losses occur in under-nappe pool circulation and seismic energy propagation.

Digital elevation modeling was highly useful for characterizing the 3-D flow structure of a horseshoe step. Despite temporal water surface fluctuations, DEMs differentiated all water surface features. This approach is suitable for field mapping natural step bed and water surface topography. Three distinct zones were evident in all DEMs- the nappe, a flow convergence zone, and a tailwater zone. When DEMs were combined with videography and hydraulics modeling, a good description of step flow dynamics was achieved.

Measurements of the planform contour curvature of the nappe suggested that flow streamtubes are not linear or radial, but somewhere in between, closer to linear, and flow dependent. The nappe centerline reasonably matched Rouse's 2-D nappe profile equation until increasing depth yielded significant hydrostatic pressure . Peripheral streamtube profiles could

not be extracted from the DEM. Due to their convergence, horseshoe-step nappe streamtubes require new profile equations with H scaled by horseshoe eccentricity and radius.

In comparison to broad-crested 2-D rectangular bed steps, the primary difference expressed by the horseshoe brink occurred in a flow convergence zone. When h_{tail} was supercritical, this zone had several features that were previously unreported, including a spray jet dome, a rooster tail, and peripheral hydraulic jumps. Such features illustrate significant organization in flow structure, even given high turbulence. No single "optimal jump" may be defined for a 3-D jump. *Ceteris paribus*, h_{tail} for full nappe-toe submergence was greater than that for a 2-D step. For the range of values explored, more diverse flow patterns with larger Z/H relief were observed for variations in h_d/H than for variations in (H+P)/H.

Even though flow processes were not quantified in detail in this study, flow aeration was observed for all runs, especially for (H+P)/H=2 and is worth discussing. Valle and Pasternack (2001) developed a field method to measure flow aeration in rivers and found it to be highly variable between sites. Such aeration is often missed in flume studies due to excessive geometric scaling, so the many potential effects of aeration have been neglected. First, flow aeration adds elasticity to water, which is otherwise inelastic. This serves to damp pressure shock waves, whether they originate from cavitation, momentum exchange in turbulent flow, jet impacts, etc. Without this effect, cavitation erosion might be significant for big steps and high flows with velocities >10 m s^{-1}. At the microscopic scale, some cavitation erosion may also occur due to local convective acceleration and associated pressure drop around multi-scalar bed roughness elements, depending on aeration level. Second, aeration can drop local hydrostatic pressure in proportion to fractional air content. When combined with positive local pressure excursions caused by jet turbulence, this effect results in a wider range of pressure variations (but not

shocks), and thus a greater potential for variation in lift force. Finally, large air pockets such as those observed for submerged jumps with (H+P)/H=2 could remove the buoyancy and viscous drag of individual cobbles and boulders impacting the bed, thereby greatly increasing the impact force on the bed. Coarse sediment may be necessary for significant bed scour and upstream step migration in highly resistant bedrock, but the role of such sediment can only be understood within the fluid mechanics context of the step. Air pockets were found to be important during the very high flows that would be transporting high loads of coarse sediment in a natural river and thus should be given greater consideration.

To motivate future research it is useful to suggest potential geomorphic processes that might result from the observed fluid mechanics. For a flow regime with a free-falling nappe, the flow over a horseshoe step will result in convergent flow. In turn, convergent flow will yield higher velocity, shear stress, and lift force differentials between the channel center and periphery. For a homogeneous bed material, this must result in greater erosion and faster headward migration at the center than at the edge. As a step migrates upstream, its brink geometry becomes increasingly eccentric. A condition will result in which the majority of the fall's periphery will approach being parallel with the channel banks (e.g. Fig. 1, main horseshoe). As the apex of the horseshoe propagates upstream, it becomes narrower and narrower, restoring flow back to the periphery. Eventually a condition may be reached when the rate of parallel migration to the banks exceeds the rate of upstream migration of the apex. A metastable balance between apex headward migration and periphery outward migration may exist. Alternately, if the concentration of flow and bedload into the center of the horseshoe results in rapid downcutting of the centerline path, then flow may become channelized with the step's periphery dried out for increasing magnitudes of flow (e.g. Monster Falls, South Santiam River, OR). Of

course, horseshoe step migration depends on bedrock resistance, fracture/jointing patterns, and bedload dynamics, complicating the generic process.

Even though field studies are unlikely to capture the range of conditions possible in controlled flumes, it is vital that efforts be made to quantify fluid mechanics at 3-D steps, because it is now clear that the existing knowledge base on 2-D hydraulics ignores the necessary range of submergence conditions as well as convergent and divergent flow patterns present in nature. Study of 2-D hydraulics alone does not provide an adequate foundation for furthering understanding of fluvial geomorphology in bedrock rivers.

8. Conclusions

This research on horseshoe steps provides new, critical information on the fluid mechanics of a common 3-D feature in bedrock rivers. The use of a large 2.75-m wide flume and discharges up to 3.47 $m^3 s^{-1}$ permitted exploration of flow dynamics at near-full scale. Digital elevation modeling, digital videography, and momentum and energy conservation modeling were used to quantify and describe convergent hydraulics below a horseshoe step. Water surface topography was found to be an essential response variable characterizing the structure of flow. The rooster tail is the essential feature of convergent flow, but with increasing tail depth it takes on the form of a boil and eventually dissipates. Peripheral flow jets become increasingly important relative to central flow convergence with increasing hydraulic jump submergence. Over 80% of total energy could be dissipated for a tall step relative to upstream specific energy. It is important to distinguish the role of a hydraulic jump in reducing velocity versus that of tail depth in controlling downstream energy and energy loss, because it has been shown that high energy loss occurs with limited reduction in velocity and vice versa (Fig. 4).

Steps with a Fr_{tail} close to critical and having no hydraulic jump will have maximal velocities and high scour associated with more energy dissipation than those with $Fr_{tail}<<1$ exhibiting strong hydraulic jumps with killer reversals.

Acknowledgements

This material is based on work supported in part by the STC Program of the National Science Foundation under Agreement number EAR-0120914, in part by the Hydrology Program of the National Science Foundation under Agreement number EAR-0207713, and in part by private funding by the lead PI- Greg Pasternack. We thank Jon Hansberger, Sara Johnson, Omid Mohseni, Gary Parker, Mike Plante, Jared Roddy, Alfredo Santana, and Jeremy Schultz for assistance with experimental setup and data collection.

References

Ackers, P., White, W., Perkins, J., Harrison, A. 1978. *Weirs and Flumes For Flow Measurement*. John Wiley & Sons: Chichester, NY, 327pp.

Alexandrowicz, Z. 1994. Geologically controlled waterfall types in the Outer Carpathians. Geomorphology 9, 155–165.

Alonso, C.V., Bennett, S.J., Stein, O. R. 2002. Predicting head cut erosion and migration in concentrated flows typical of upland areas, Water Resour. Res. 38 (12), 1303, doi:10.1029/2001WR001173.

Bennett, S.J., 1999. Effect of slope on the growth and migration of headcuts in rills. Geomorphology 30, 273-290.

Bennett, S.J. and Casali, J. 2001. Effect of initial step height on headcut development in upland concentrated flows. Water Resour. Res. 37 (5), 1475-1484.

Bennett, S.J., Alonso, C.V., Prasad, S.N., Römkens, M.J.M. 2000. Experimentsd on headcut growth and migration in concentrated flows typical of upland areas. Water Resour. Res. 36 (7), 1911-1922.

Bollart, E., Schleiss, A. 2003a. Scour of rock due to the impact of plunging high velocity jets Part I: a state-of-the-art review. J. Hydraul. Res. 41:5:451-464.

Bollart, E., Schleiss, A. 2003b. Scour of rock due to the impact of plunging high velocity jets part II: experimental results of dynamic pressures at pool bottoms and in one- and two-dimensional closed end rock joints. J. Hydraul. Res. 41 (5), 465-480.

Brasington J., Rumsby B.T., McVey R.A. 2000. Monitoring and modelling morphological change in a braided gravel-bed river using high resolution GPS-based survey. Earth Surf. Processes and Landforms 25 (9), 973-990.

Chanson, H. 1995. *Hydraulic Design of Stepped Cascades, Channels, Weirs and Spillways*. Pergamon: Oxford, UK, 292pp.

Chanson, H. 1999. *The Hydraulics of Open Channel Flow*. Arnold: London, 495pp.

Chanson, H. 2002. *The Hydraulics of Stepped Chutes and Spillways*. A.A. Balkema Publishers: Lisse. 384pp.

Chanson, H., Toombes, L. 1998. Supercritical flow at an abrupt drop: flow patterns and aeration. Can. J. Civil Eng. 25, 956-966.

Coleman, S.E., Melville, B.W., Gore, L. 2003. Fluvial entrainment of protruding fractured rock. J. Hydraul. Eng. 129 (11), 872-884.

Comiti, F., Lenzi, M.A., Marion, A. 2002. Local scour at grade-control structures in mountain rivers: laboratory and field data. (Bousmar, D. and Zech, Y., eds.) River Flow 2002, Proceedings of the international conference on fluvial hydraulics, Louvain-La-Neuve, Belgium, p. 1073-1078.

Derricourt, R.M. 1976. Retrogression rate of the Victoria Falls and the Batoka Gorge. Nature 264, 23–25.

Elevatorski, E.A. 1959. *Hydraulic Energy Dissipators*. McGraw-Hill Book Company: New York, NY, 214pp.

Falvey, H.T. 2003. *Hydraulic Design of Labyrinth Weirs*. American Society of Civil Engineers: Reston, VA, 162pp.

Fiorotoo, V., Rinaldo, A. 1992. Fluctuating uplift and lining design in spillway stilling basins. J. Hydraul. Eng. 118(4), 578-596.

Hanson, G.J., Robinson, K.M., Cook, K.R. 1997. Headcut migration analysis of a compacted soil. Trans. ASAE 40 (2), 355–361.

Hayakawa, Y., Matsukura, Y. 2003. Recession rates of waterfalls in Boso Peninsula, Japan, and a predictive equation. Earth Surf. Processes and Landforms 28 (6), 675-684.

Henderson, F.M. 1966. *Open Channel Flow*. Macmillan: New York, NY, p.79-228.

Lane, S.N, Chandler, J.H., Richards, K.S. 1994. Developments in monitoring and modeling small-scale river bed topography. Earth Surf. Processes and Landforms 19 (4), 349-368.

Lenzi, M.A., Comiti, F. 2003.Local scouring and morphological adjustments in steep channels. Geomorphology 55, 97–109.

Lenzi, M.A., Marion, A., Comiti, F. 2003b. Local scouring at grade-control structures in alluvial mountain rivers. Water Resour. Res. 39 (7), 1176, doi:10.1029/2002WR001815.

Lenzi, M.A., Marion, A., Comiti, F. 2003a. Interference processes on scouring at bed sills. Earth Surf. Processes and Landforms 28 (1), 99-110.

Lenzi, M.A., Marion, A., Comiti, F., Gaudio, R. 2002. Local scouring in low and high gradient streams at bed sills. J. Hydraul. Res. 40 (6), 731-739.

Leutheusser, H.J., Birk, W.M. 1991. Drownproofing of low overflow structures. J.Hydraul. Eng. 117 (2), 205-213.

Moore, J.S. 1997. Field procedures for the headcut erodibility index. Trans. ASAE 40 (3), 563–574.

Mossa, M., Petrillo, A., Chanson, H. 2003. Tailwater level effects on flow conditions at an abrupt drop. J. Hydraul. Res. 41, 39-51.

Parker, G., Izumi, N. 2000. Purely erosional cyclic and solitary steps created by flow over a cohesive bed. G. Parker and N. Izumi. J. Fluid Mech. 419, 203-238.

Rand, W. 1955. Flow geometry at straight drop spillways. Proc. ASCE 81 (791), 1-13.

Robinson, K.M., 1992. Predicting stress and pressure at an overfall. Trans. ASAE 35 (20, 561–569.

Robinson, K. M. and Hanson, G. J. 1996. Gully headcut advance. Trans. of the ASAE. 39(1):33-38.

Robinson, K.M., Hanson, G.J., Cook, K.R., Kadavy, K.C. 2001. Erosion of fractured materials. Trans. ASAE 44 (4), 819–823.

Rouse, H. 1957. *Elementary Mechanics of Fluids*: John Wiley, New York.

Simon, A., Thomas, R.E. 2002. Processes and forms of an unstable alluvial system with resistant, cohesive streambeds. Earth Surf. Processes and Landforms 27, 699-718.

Sklar, L.S., Dietrich, W.E. 2001. Sediment and rock strength controls on river incision into bedrock. Geology 29:12:1087-1090.

Stein, O.R., Julien, P.Y. 1993. Criterion delineating the mode of headcut migration. J.Hydraul. Eng. 119 (1), 37-50.

Stein, O.R.,Julien, P.Y., Alonso, C.V. 1993. Mechanics of jet scour downstream of a headcut. J. Hydraul. Res. 31(6), 723-738.

Stein, O.R., LaTray, D.A. 2002. Experiments and Modeling of Headcut Migration in Stratified Soils. Water Resour. Res. 38 (12), 1284:doi:10.1029/2001WR001166.

Tinkler, K.J., Pengelly, J.W., Parkins, W.G., Asselin, G. 1994. Postglacial recession of Niagara Falls in relation to the Great Lakes. Quart. Res. 42, 20-29.

United States Bureau of Reclamation. 1948. Studies of crests for overfall dams. Boulder Canyon Project Final Reports, Part VI- Hydraulic Investigations, Bulletin 3.

Vallé. B.L., Pasternack, G.B. 2001. TDR measurements of hydraulic jump aeration in the South Fork of the American River, CA. Geomorphology 42, 153-165.

Vischer, D.L., Hager, W.H. 1998. *Dam hydraulics*. John Wiley & Sons: Chichester, NY, 316pp.

White, M.P. 1943. Energy loss at the base of a free overfall- discussion. Trans. ASCE, 108, 1361-1364.

Wohl, E.E., Grodek, T. 1994. Channel bed-steps along Nahal Yael, Negev desert, Israel. Geomorphology 9 (2), 117-126.

Table 1. Summary of experimental run conditions grouped by energy.

	Upstream Flow Conditions							Downstream Flow Conditions			
Run	H (m)	(H+P)/H	H/P	H/L	Q (cumecs)*	h_{up} (m)*	V_{up} (m s^{-1})*	h_d/H	h_t/H	V_{tail} (m s^{-1})*	$h_L/(H+P)$*
(H+P)/H=5.55											
1	0.201	5.55	0.22	0.05	0.36	1.11	0.12	5.23	0.32	2.03	0.75
2	0.201	5.55	0.22	0.05	0.36	1.11	0.12	3.72	1.83	0.35	0.66
3	0.201	5.55	0.22	0.05	0.36	1.11	0.12	3.05	2.5	0.26	0.55
4	0.201	5.55	0.22	0.05	0.36	1.11	0.12	1.88	3.67	0.18	0.34
(H+P)/H=4.75											
5	0.244	4.75	0.27	0.06	0.48	1.16	0.15	4.41	0.34	2.10	0.73
6	0.244	4.75	0.27	0.06	0.48	1.16	0.15	3.01	1.74	0.41	0.63
7	0.244	4.75	0.27	0.06	0.48	1.16	0.15	2.4	2.35	0.30	0.50
8	0.244	4.75	0.27	0.06	0.48	1.16	0.15	1.45	3.3	0.22	0.30
(H+P)/H=4.00											
9	0.305	4.00	0.33	0.07	0.67	1.22	0.20	3.67	0.33	2.42	0.67
10	0.305	4.00	0.33	0.07	0.67	1.22	0.20	2.54	1.46	0.55	0.62
11	0.305	4.00	0.33	0.07	0.67	1.22	0.20	2.01	1.99	0.40	0.50
12	0.305	4.00	0.33	0.07	0.67	1.22	0.20	1.38	2.62	0.30	0.34
13	0.305	4.00	0.33	0.07	0.67	1.22	0.20	1.14	2.86	0.28	0.28
(H+P)/H=3.00											
14	0.457	3.00	0.50	0.11	1.23	1.37	0.33	2.67	0.33	2.96	0.56
15	0.457	3.00	0.50	0.11	1.23	1.37	0.33	1.58	1.42	0.69	0.51
16	0.457	3.00	0.50	0.11	1.23	1.37	0.33	1.42	1.58	0.62	0.46
17	0.457	3.00	0.50	0.11	1.23	1.37	0.33	1.26	1.74	0.56	0.41
18	0.457	3.00	0.50	0.11	1.23	1.37	0.33	0.81	2.19	0.45	0.26
(H+P)/H=2.00											
19	0.914	2.00	1.00	0.21	3.47	1.80	0.69	1.63	0.37	3.74	0.43
20	0.914	2.00	1.00	0.21	3.47	1.80	0.69	0.91	1.09	1.27	0.41
21	0.914	2.00	1.00	0.21	3.47	1.80	0.69	0.74	1.26	1.10	0.34

Step dimensions: P=0.914 m, R=1.372 m, width=2.743 m, length=4.28 m

*These values calculated using equations 1-6

Table 2. Non-dimensional coordinates of key points along the channel centerline.

specified run		step brink		nappe toe		rooster or boil apex	
hd/H	ht/H	X/H	Z/H	X/H	Z/H	X/H	Z/H
(H+P)/H=5.55							
5.23	0.32	0.000	5.214	3.574	0.420	12.974	1.695
3.72	1.83	0.000	5.214	2.899	1.270	9.655	2.134
3.05	2.5	0.000	5.214	2.686	2.305	8.645	2.736
1.88	3.67	0.000	5.214	1.856	3.507	6.609	3.724
(H+P)/H=4.75							
4.41	0.34	0.000	4.363	3.021	0.438	10.640	1.554
3.01	1.74	0.000	4.363	2.923	1.323	8.864	1.909
2.40	2.35	0.000	4.363	2.332	2.113	8.636	2.420
1.45	3.3	0.000	4.363	1.673	3.145	7.696	3.369
(H+P)/H=4.00							
3.67	0.33	0.000	3.580	3.386	0.295	8.972	1.391
2.54	1.46	0.000	3.580	2.680	0.749	7.143	1.741
2.01	1.99	0.000	3.580	2.137	1.681	6.736	2.080
1.38	2.62	0.000	3.580	1.689	2.402	6.469	2.684
1.14	2.86	0.000	3.580	1.483	2.661	6.470	2.852
(H+P)/H=3.00							
2.67	0.33	0.000	2.528	2.668	0.374	7.683	0.954
1.58	1.42	0.000	2.528	1.992	0.962	6.358	1.514
1.42	1.58	0.000	2.528	1.718	1.247	6.313	1.589
1.26	1.74	0.000	2.528	1.564	1.496	7.278	1.728
0.81	2.19	0.000	2.528	1.085	2.006	8.484	2.144
(H+P)/H=2.00							
1.63	0.37	0.000	1.459	1.662	0.381	4.066	0.632
0.91	1.09	0.000	1.459	1.362	0.507	4.275	1.099
0.74	1.26	0.000	1.459	0.9236	0.97053	n/a	n/a

Figure Captions

Figure 1. Aerial and oblique photos of 4.5-m high Shanghai Falls on the Feather River, California, USA illustrating the lateral complexity of the horseshoe configuration.

Figure 2. Definition sketch of flow profile over a bread-crested, ventilated step.

Figure 3. Plots of a) energy and b) energy loss for an optimal jump below an abrupt drop.

Figure 4. Fractional energy loss for a range of non-dimensional upstream energy and downstream submergence. Points are the experimental conditions investigated in this study.

Figure 5. Photos of a) experimental broad-crested horseshoe step and b) data acquisition system over the falls.

Figure 6. Photos (a,b) and DEMs (c-f) for (H+P)/H=5.55 runs, with ht/H= a,c) 0.32, b,e) 1.83, d) 2.5, and f) 3.67.

Figure 7. Centerline profiles for all runs, with (H+P)/H= a) 5.55, b) 4.75, c) 4.00, d) 3.00, and e) 2.00.

Figure 8. Photos (a,b) and DEMs (c-f) for (H+P)/H=4.75 runs, with ht/H= a,e) 2.35, b,c) 0.32, d) 1.74, and f) 3.30.

Figure 9. DEMs for (H+P)/H=4 runs, with ht/H= a) 0.33, b) 1.46, c) 1.99, d) 2.62, and e) 2.86.

Figure 10. DEMs for (H+P)/H=3 runs, with ht/H= a) 0.33, b) 1.42, c) 1.58, d) 1.74, and e) 2.19.

Figure 11. DEMs for (H+P)/H=2 runs, with ht/H= a) 0.37, b) 1.09, c) 1.26.

Figure 12. Non-dimensional centerline nappe profiles: a) measured profiles and b) measured profiles shifted to common datum and fitted with Rouse's nappe profile equation.

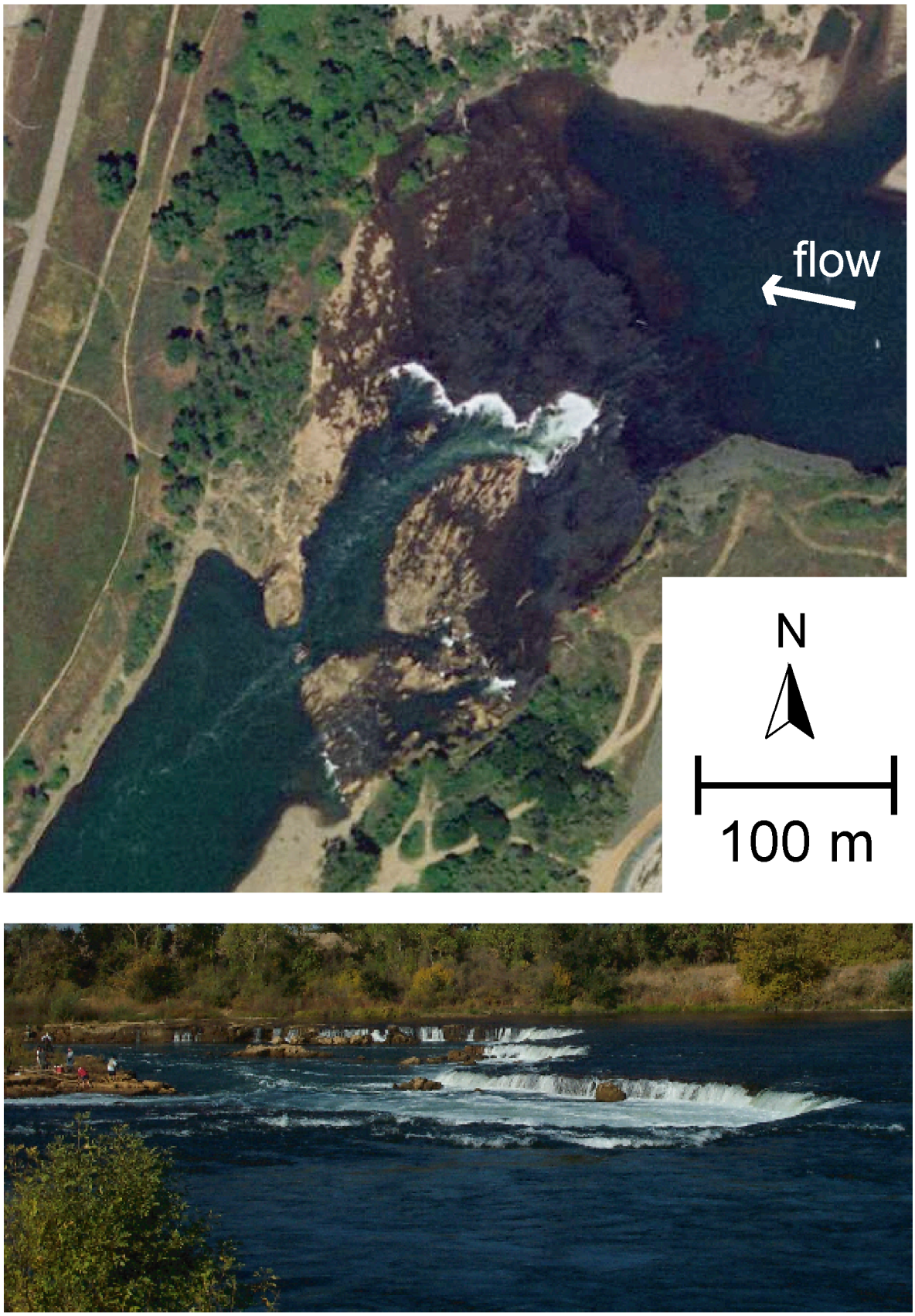

Figure 1.

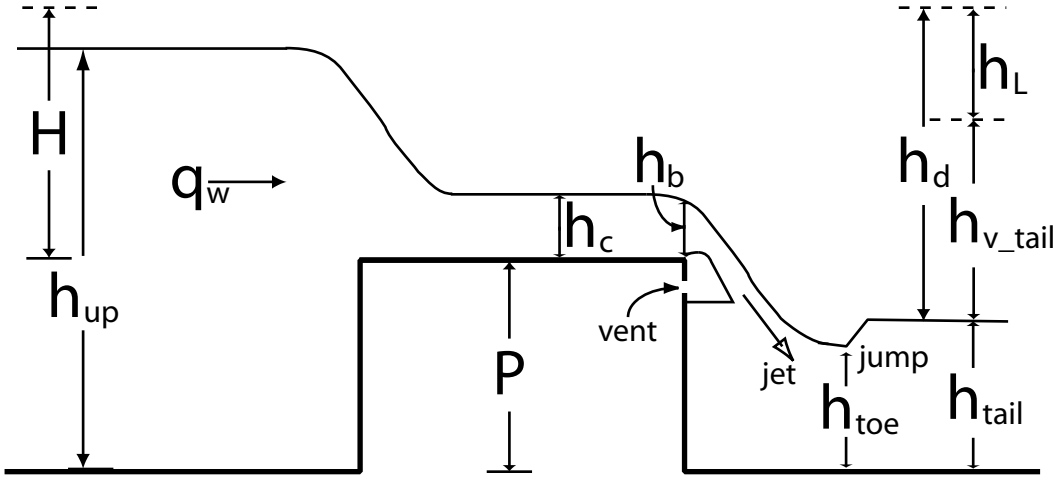
H
q_w
h_{up}
h_c
h_b
P
vent
jet
jump
h_{toe}
h_L
h_d
h_{v_tail}
h_{tail}

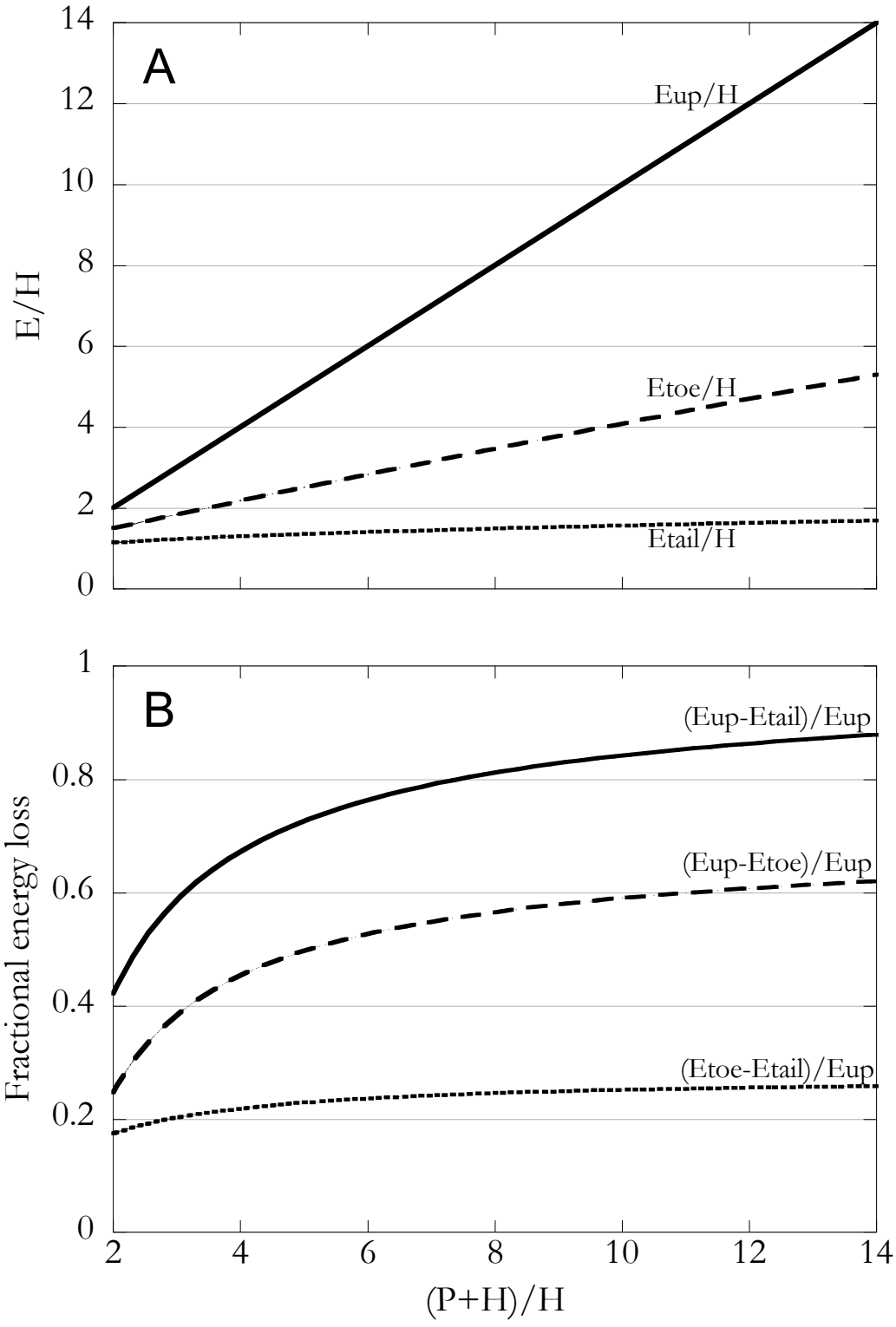
A
Eup/H
Etoe/H
Etail/H
E/H
0
2
4
6
8
10
12
14
B
(Eup-Etail)/Eup
(Eup-Etoe)/Eup
(Etoe-Etail)/Eup
Fractional energy loss
0
0.2
0.4
0.6
0.8
1
2
4
6
8
10
12
14
(P+H)/H

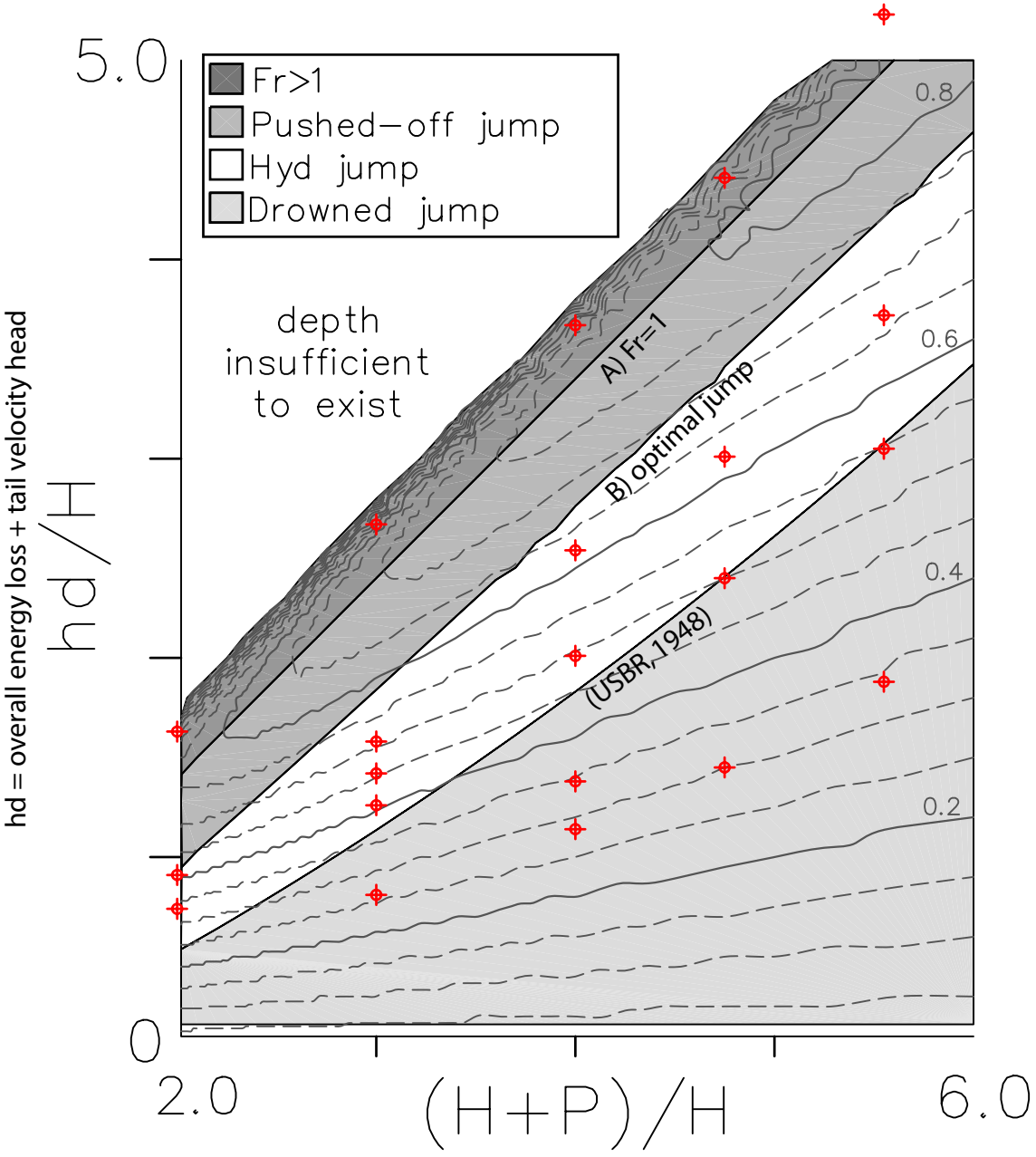
5.0
0
2.0
6.0
(H+P)/H
hd/H
hd = overall energy loss + tail velocity head
Fr>1
Pushed–off jump
Hyd jump
Drowned jump
depth
insufficient
to exist
A) Fr=1
B) optimal jump
(USBR,1948)
0.8
0.6
0.4
0.2

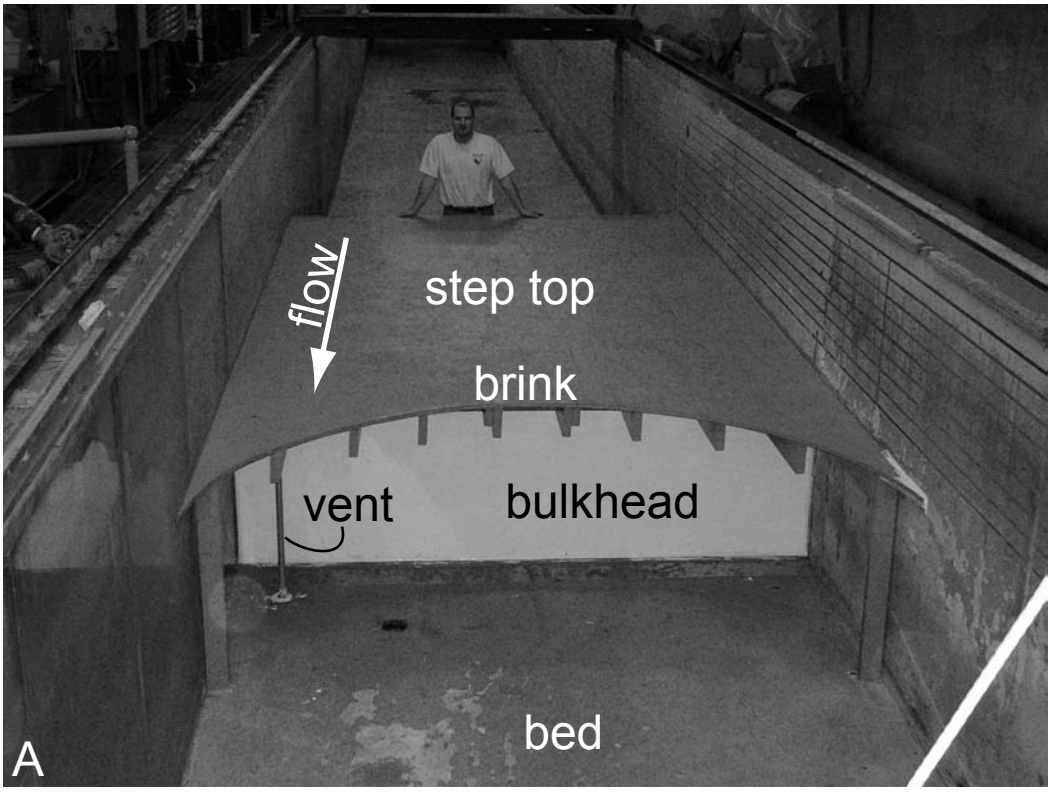
flow
step top
brink
vent
bulkhead
bed
A


B

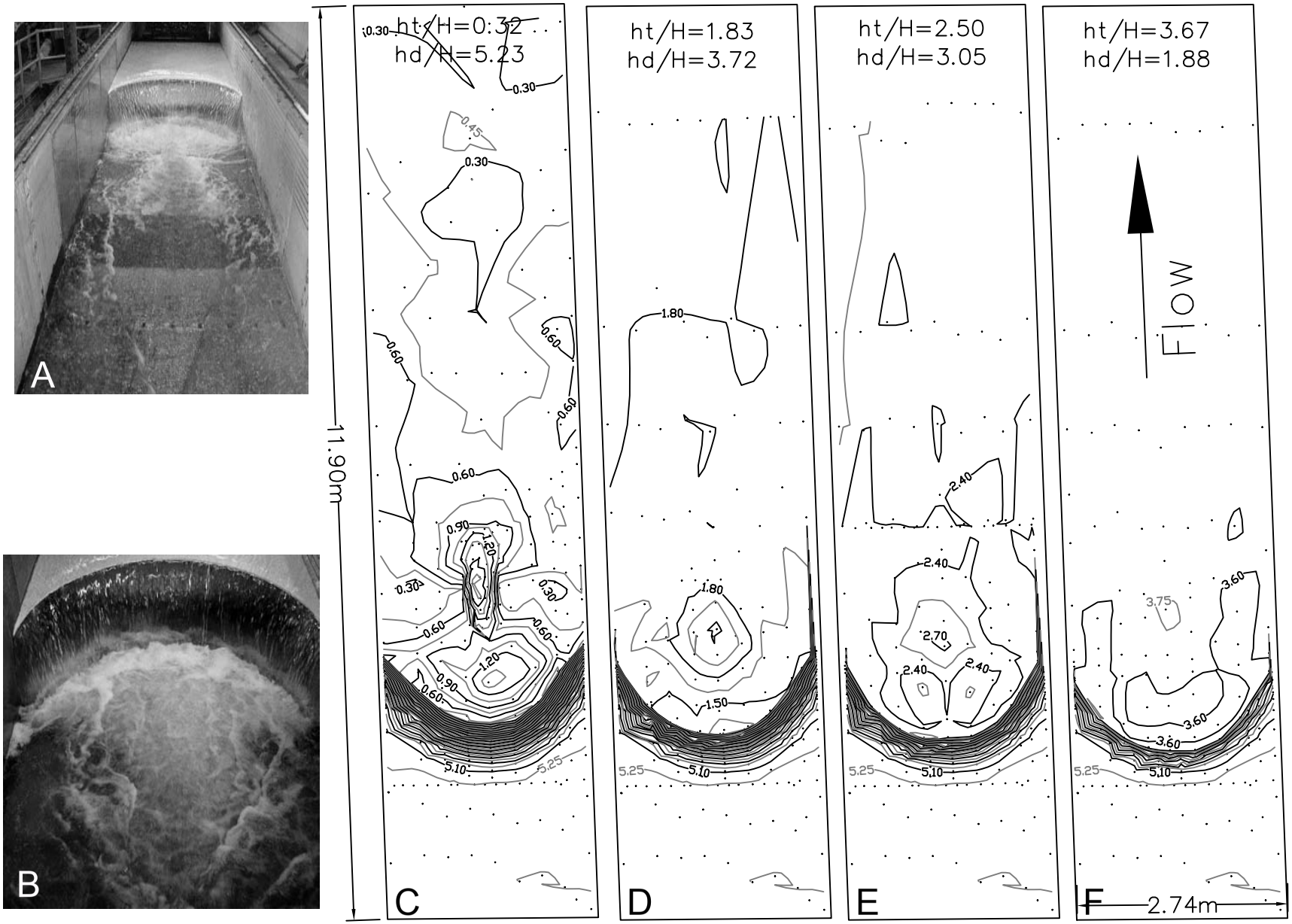
A
B
C
D
E
F
ht/H=0.32
hd/H=5.23
ht/H=1.83
hd/H=3.72
ht/H=2.50
hd/H=3.05
ht/H=3.67
hd/H=1.88
11.90m
Flow
2.74m
0.30
0.45
0.60
0.90
1.20
1.50
1.80
2.40
2.70
3.60
3.75
5.10
5.25

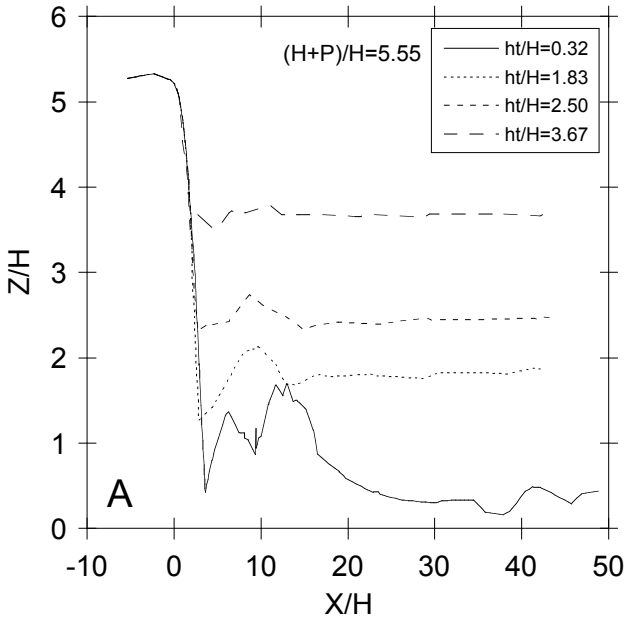
(H+P)/H=5.55
ht/H=0.32
ht/H=1.83
ht/H=2.50
ht/H=3.67
A
Z/H
X/H

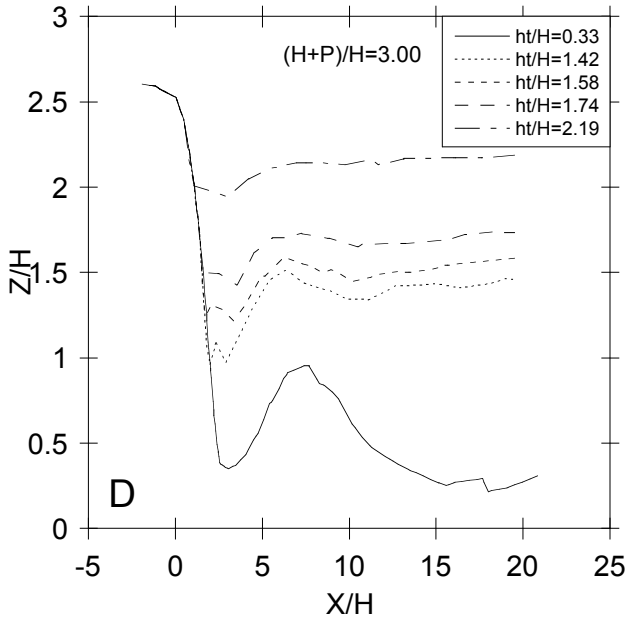
(H+P)/H=3.00
ht/H=0.33
ht/H=1.42
ht/H=1.58
ht/H=1.74
ht/H=2.19
D
Z/H
X/H

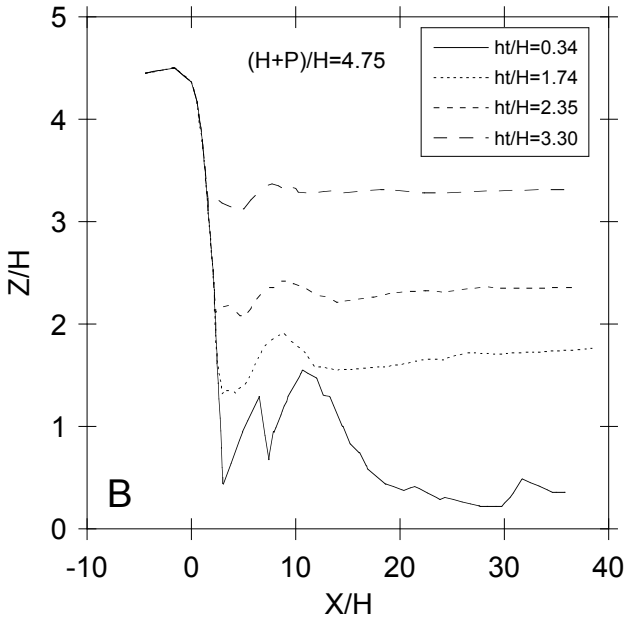
(H+P)/H=4.75
ht/H=0.34
ht/H=1.74
ht/H=2.35
ht/H=3.30
B
Z/H
X/H

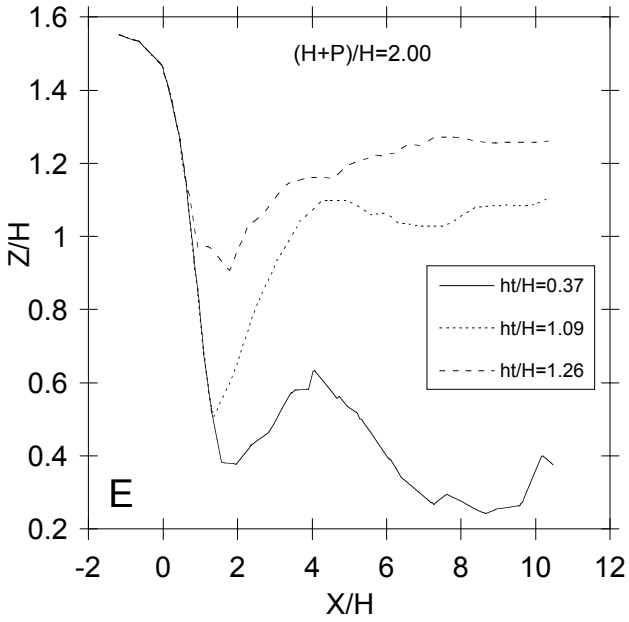
(H+P)/H=2.00
ht/H=0.37
ht/H=1.09
ht/H=1.26
E
Z/H
X/H

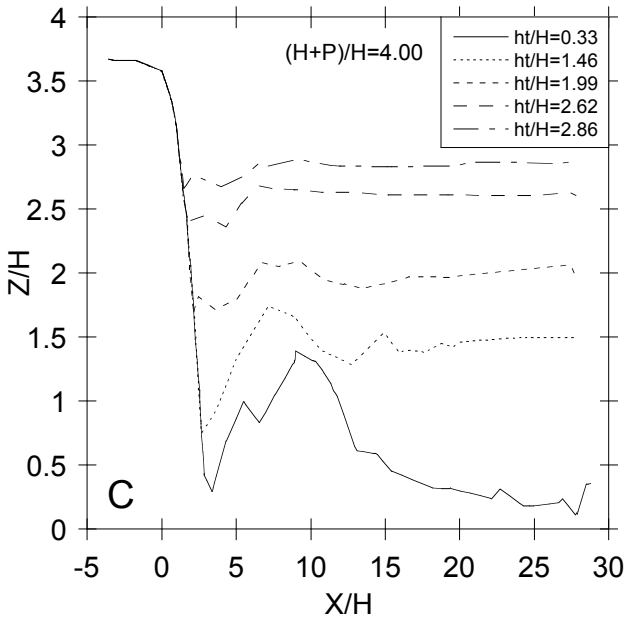
(H+P)/H=4.00
ht/H=0.33
ht/H=1.46
ht/H=1.99
ht/H=2.62
ht/H=2.86
C
Z/H
X/H

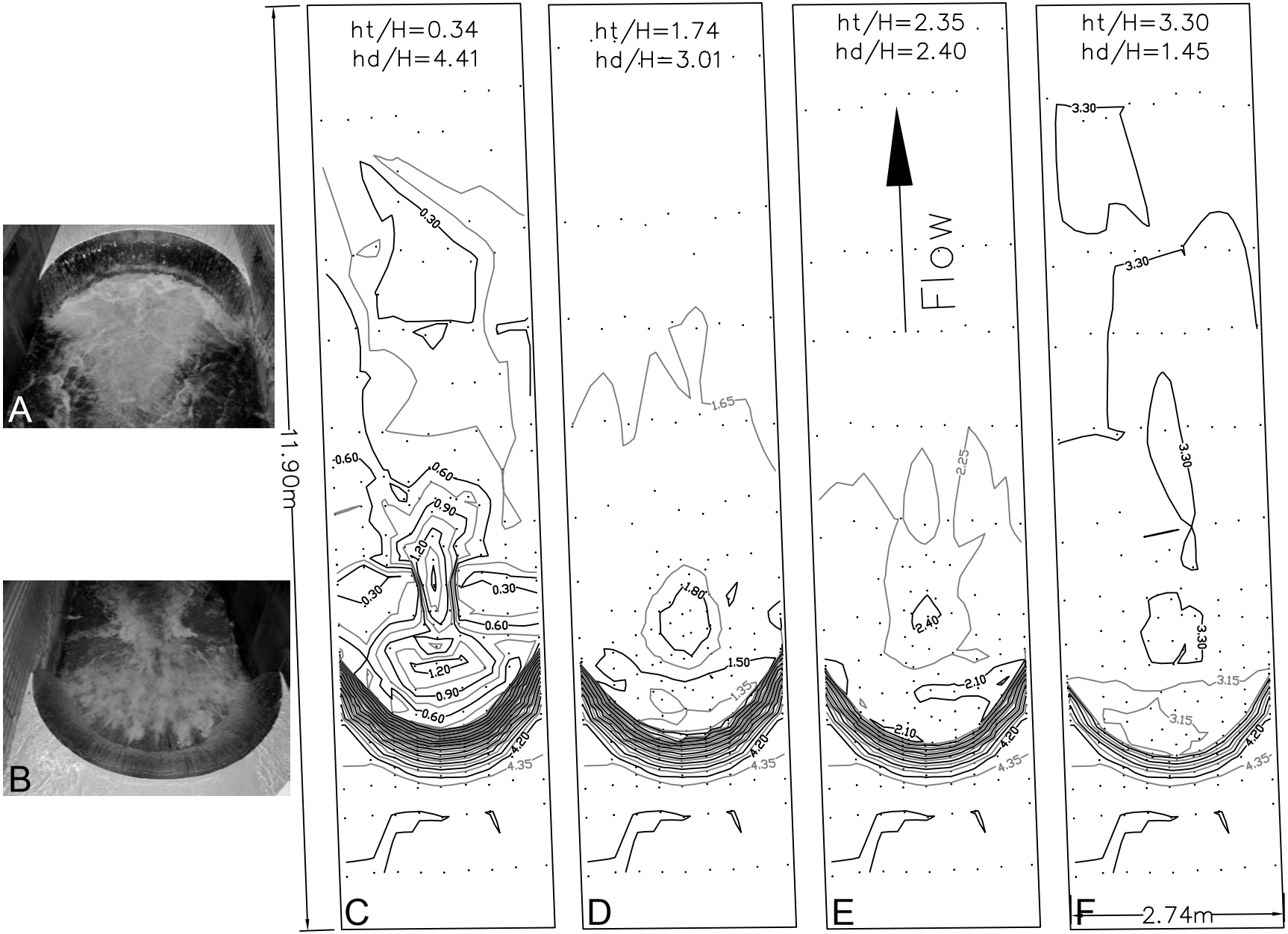
A
B
11.90m
ht/H=0.34
hd/H=4.41
ht/H=1.74
hd/H=3.01
ht/H=2.35
hd/H=2.40
ht/H=3.30
hd/H=1.45
Flow
C
D
E
F
2.74m

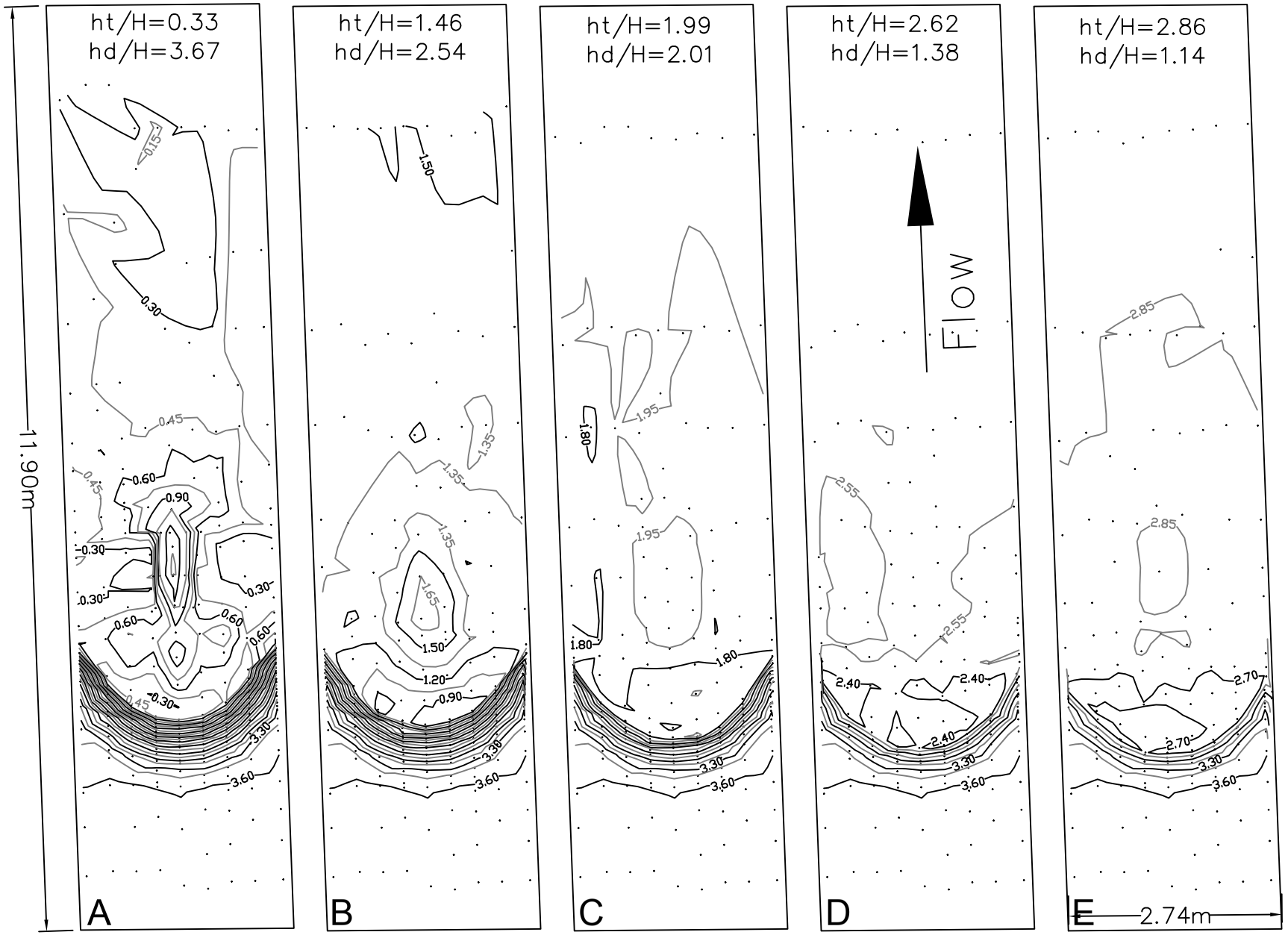
ht/H=0.33
hd/H=3.67
ht/H=1.46
hd/H=2.54
ht/H=1.99
hd/H=2.01
ht/H=2.62
hd/H=1.38
ht/H=2.86
hd/H=1.14
Flow
11.90m
2.74m
A
B
C
D
E

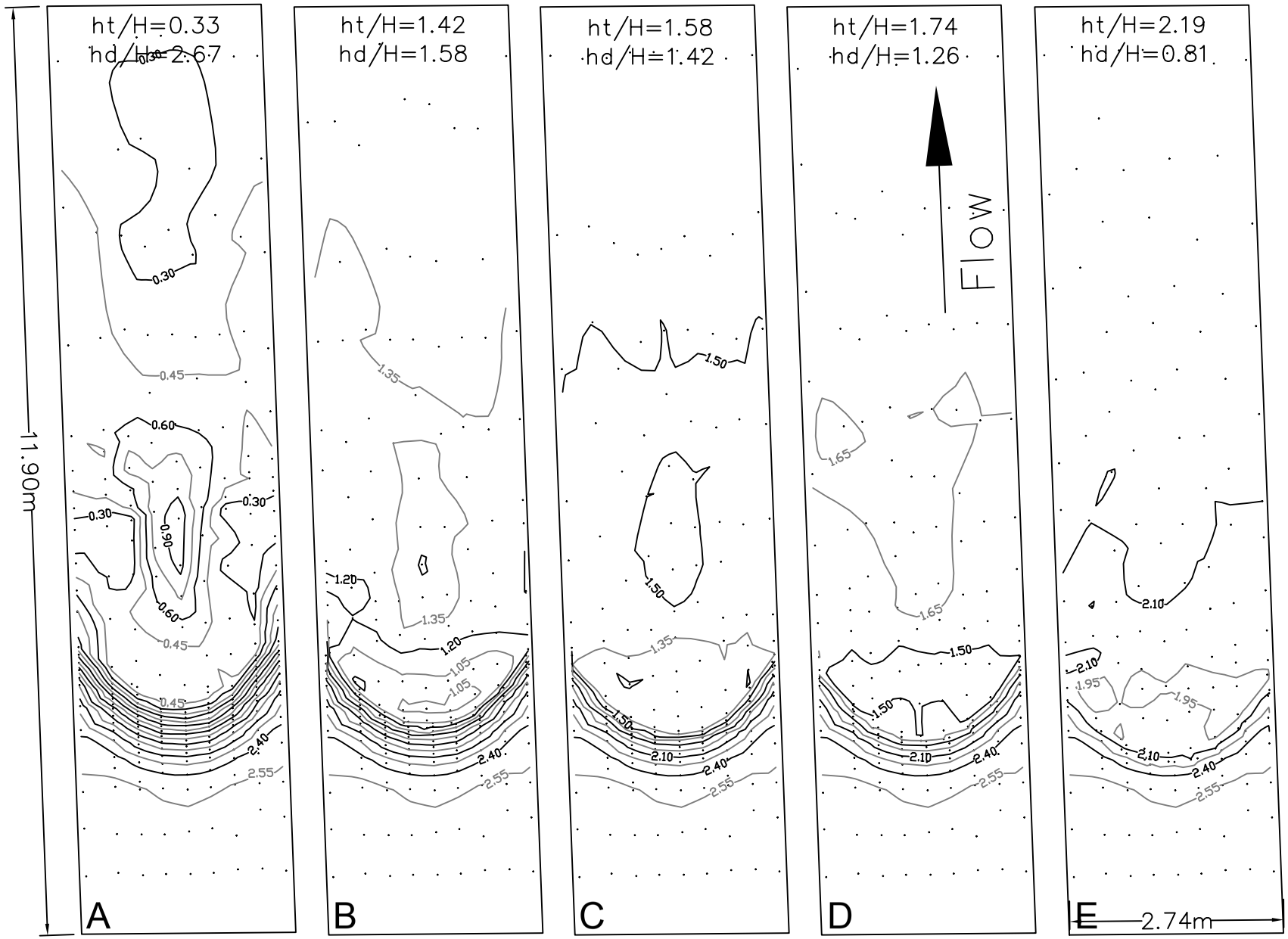
ht/H=0.33
hd/H=2.67
ht/H=1.42
hd/H=1.58
ht/H=1.58
hd/H=1.42
ht/H=1.74
hd/H=1.26
ht/H=2.19
hd/H=0.81
Flow
11.90m
2.74m
A
B
C
D
E
0.30
0.45
0.60
0.90
1.20
1.35
1.05
1.50
1.65
1.95
2.10
2.40
2.55

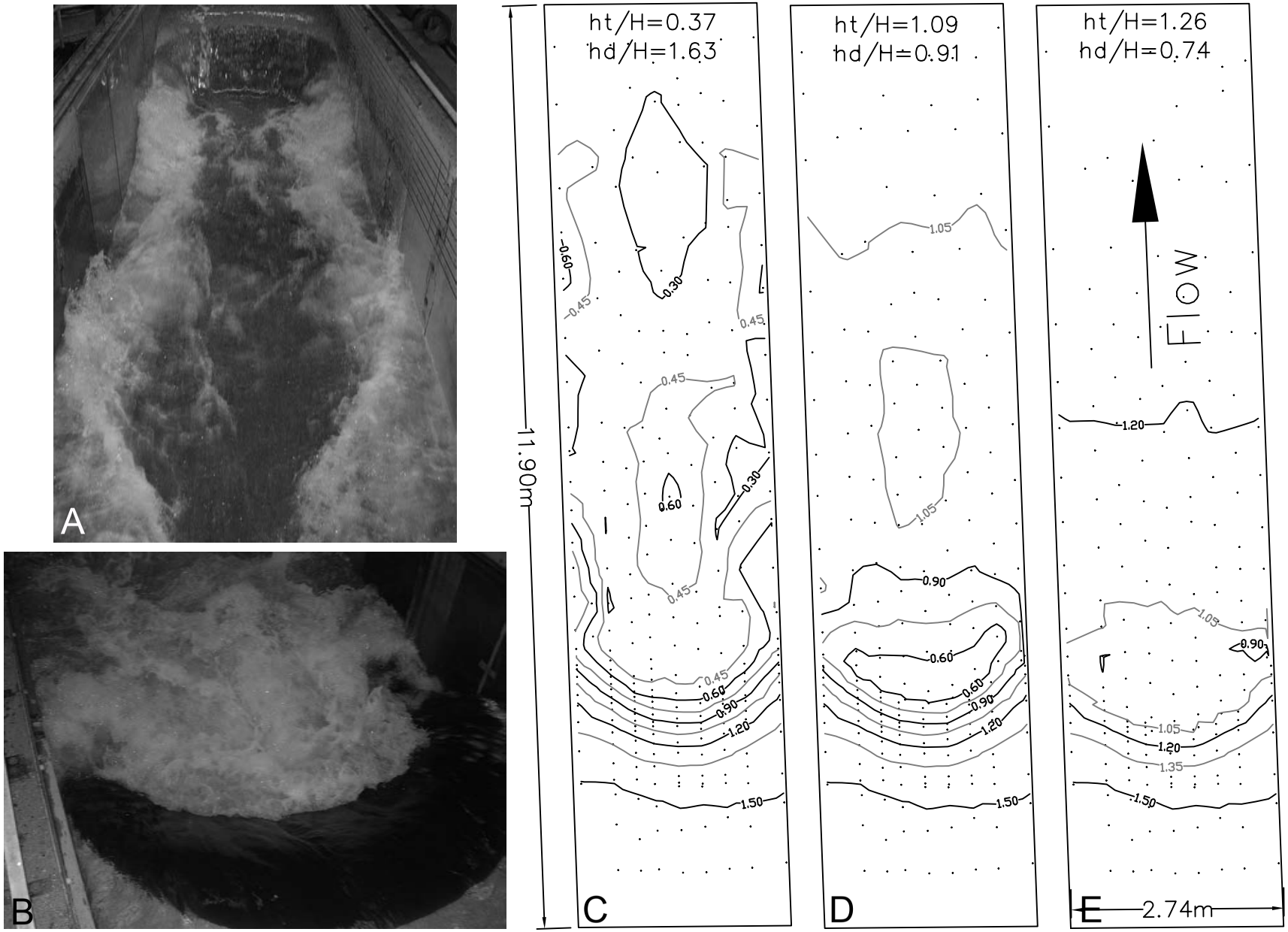
A
B
ht/H=0.37
hd/H=1.63
ht/H=1.09
hd/H=0.91
ht/H=1.26
hd/H=0.74
11.90m
Flow
C
D
E
2.74m
0.30
0.45
0.60
0.90
1.05
1.20
1.35
1.50

A)

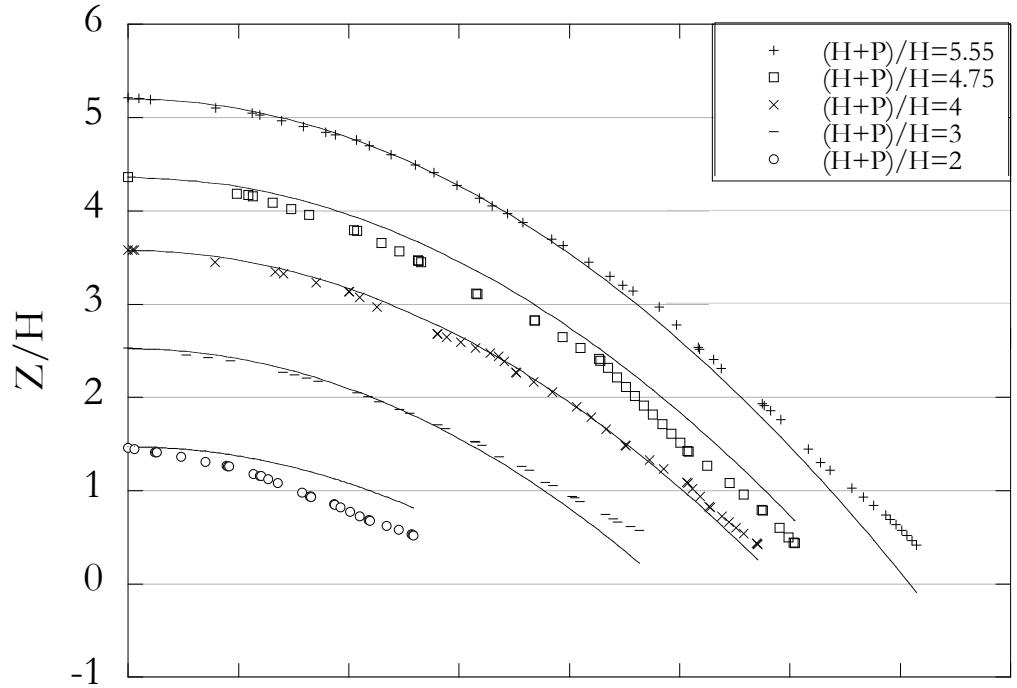
(H+P)/H=5.55
(H+P)/H=4.75
(H+P)/H=4
(H+P)/H=3
(H+P)/H=2
Z/H
6
5
4
3
2
1
0
-1

B)

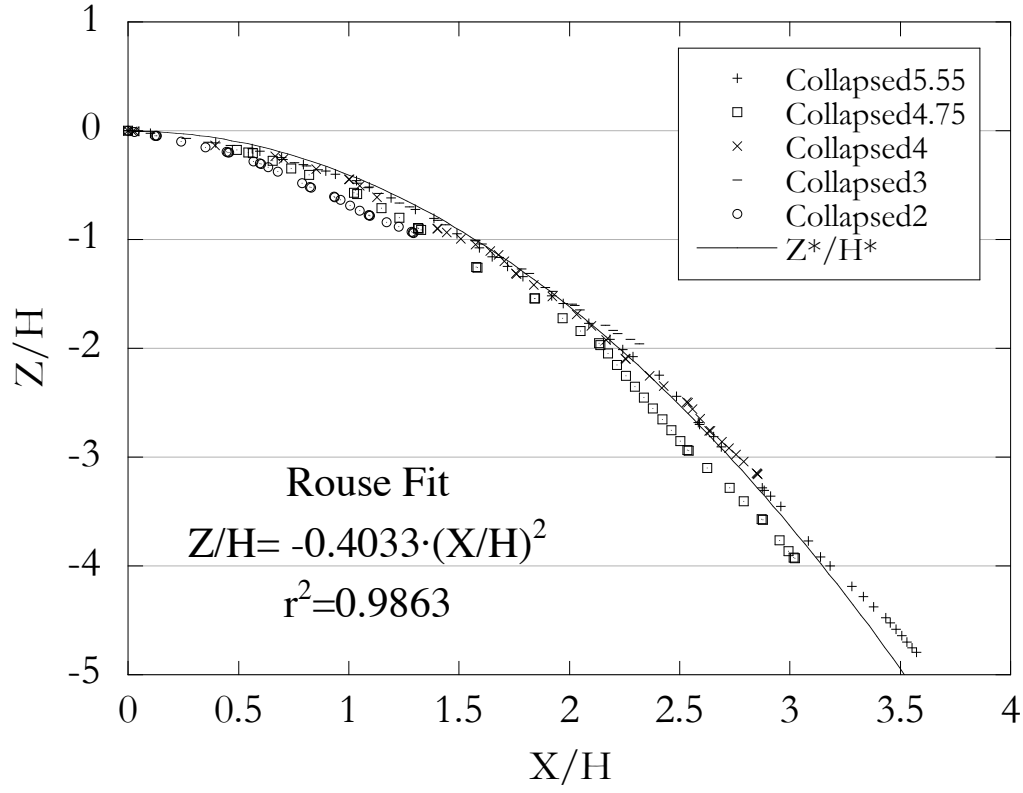
Collapsed5.55
Collapsed4.75
Collapsed4
Collapsed3
Collapsed2
Z*/H*
Rouse Fit
Z/H= -0.4033·(X/H)2
r2=0.9863
Z/H
X/H
1
0
-1
-2
-3
-4
-5
0
0.5
1
1.5
2
2.5
3
3.5
4